

Head and Neck Dynamics: Prediction of Sports Related Head Impact Characteristics

by

Callie Rennae Frantz

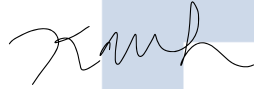
Copyright © Callie Rennae Frantz 2022

A Thesis Submitted to the Faculty of the
DEPARTMENT OF BIOMEDICAL ENGINEERING
In Partial Fulfillment of the Requirements
For the Degree of
MASTER OF SCIENCE
In the Graduate College
THE UNIVERSITY OF ARIZONA

2022

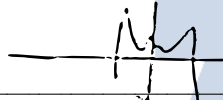
THE UNIVERSITY OF ARIZONA
GRADUATE COLLEGE

As members of the Master’s Committee, we certify that we have read the thesis prepared by Callie Frantz, titled Head and Neck Dynamics: Prediction of Sports Related Head Impact Characteristics and recommend that it be accepted as fulfilling the dissertation requirement for the Master’s Degree.



Kaveh Laksari, Ph.D.

Date: August 16, 2022



Samy Missoum, Ph.D.

Date: August 16, 2022

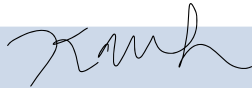


Zong-Ming Li, Ph.D.

Date: August 16, 2022

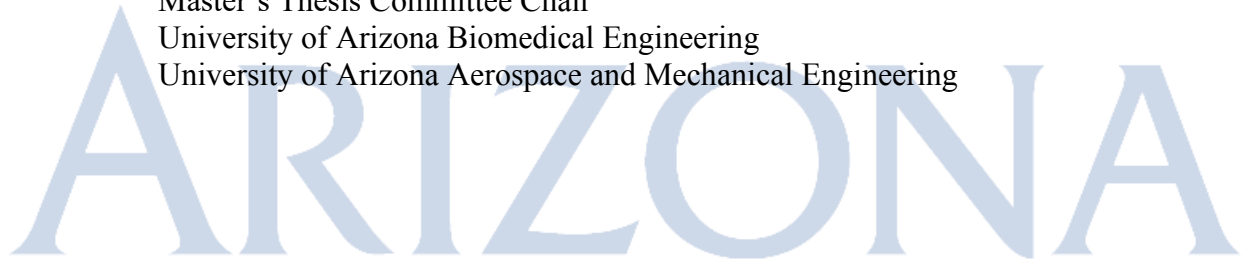
Final approval and acceptance of this thesis is contingent upon the candidate’s submission of the final copies of the thesis to the Graduate College.

I hereby certify that I have read this thesis prepared under my direction and recommend that it be accepted as fulfilling the Master’s requirement.



Kaveh Laksari, Ph.D
Master’s Thesis Committee Chair
University of Arizona Biomedical Engineering
University of Arizona Aerospace and Mechanical Engineering

Date: August 16, 2022 



ACKNOWLEDGEMENTS

I would like to acknowledge and extend thanks to Kaveh Laksari, PhD, my advisor for my thesis research, my thesis committee, and the friends and colleagues I have made throughout my graduate student career. Dr. Laksari and his laboratory presented a wonderful research opportunity that I am grateful I pursued. I would also like thank all of my lab mates for their encouragement, feedback, and support; they were instrumental in helping me find a solution when I encountered research roadblocks.

DEDICATION

This work is dedicated to my family; without their constant support, none of this would have been possible. My husband, Jonathan, is one of my greatest blessings, his mathematical expertise and endless encouragement saw me through. My brothers, Gavin and Riley, set high bars for me to reach, and have always been my heroes. My parents, they have been everything, all that I have accomplished is due to them; I am especially grateful to Mom, I treasure every moment we had.

TABLE OF CONTENTS

LIST OF FIGURES	7
LIST OF TABLES	8
LIST OF ABBREVIATIONS	9
ABSTRACT	10
INTRODUCTION	11
CHAPTER 1: Head Impact Biomechanics	13
1.1 Real-World Impacts	13
1.1.1 Kinematic Data Collection.....	13
1.1.2 Video Analysis	14
1.2 Impact Recreation	15
1.3 Injury Analysis	16
1.3.1 Injury Metrics.....	16
1.3.2 Finite Element Analysis	17
1.4 Research Focus	18
CHAPTER 2: Impact Device.....	19
2.1 Background	19
2.2 Impact Device Design.....	19
2.2.1 Design Considerations	19
2.2.2 Force Analysis.....	21
2.2.6 Pendulum Control	23
2.3 Anthropomorphic Testing Device (ATD).....	23
2.3.1 Biokinetics Target Table.....	24
2.3.2 Hybrid III Neck.....	24
2.3.3 NOCSAE Head Form	25
2.4 Data Collection	27
2.4.1 Kinematic Data	27
2.4.2 Force Data	28
2.4.3 High-Speed Video	28
2.4.4 Data Acquisition.....	29
CHAPTER 3: Mathematical Model.....	30
3.1 Rigid Link Model.....	30
3.1.1 Euler-Lagrange Dynamics	31
3.1.2 Moment Cross Products.....	34
CHAPTER 4: Experimental Methods.....	35
4.1 Test Matrix	35

4.1.1 Sport Selection	35
4.1.2 Impact Locations.....	35
4.1.3 Impact Categories	36
4.2 Signal Processing.....	38
4.3 Model Parameters	39
4.4 Predicting Impact Location.....	41
CHAPTER 5: Results	43
5.1 Kinematic Measurements.....	43
5.2 Model Parameters	44
5.3 Dynamic Predictions.....	45
5.3.1 Helmeted Impact Predictions.....	46
5.3.2 Unprotected Impact Predictions.....	48
5.3.3 Statistical and Error Analysis.....	50
CHAPTER 6: Discussion.....	52
6.1 Discussion.....	52
6.2 Limitations	53
6.3 Future Directions	54
CONCLUSION.....	55
Appendix I	56
Pendulum Assembly.....	56
Appendix II	57
Deriving Euler-Lagrange Dynamics	57
Appendix III.....	60
FIR Design Filter Derivative	60
Defining location of impact	61
Appendix IV.....	63
Exploratory Data Analysis	63
Supplementary Data.....	64
REFERENCES	65

LIST OF FIGURES

Figure 1: SOLIDWORKS® rendering of the complete pendulum design.	20
Figure 2: Variable mass and end cap for pendulum arm.....	21
Figure 3: NOCSAE head form on Hybrid III neck.....	24
Figure 4: Custom head-neck attachment.....	25
Figure 5: Assembled impact test device.....	26
Figure 6: a) DTS 6DX Pro on custom mount b) 6DX Pro mounted inside NOCSAE Head.....	27
Figure 7: Load cell placement on impactor between endcap and steel plates.	28
Figure 8: Overlay of high-speed video stills to capture the motion of the head.....	28
Figure 9: Data acquisition setup using DTS SLICEWare and SLICE Micro Stacks.....	29
Figure 10: Rigid link manipulator model, coordinate system and generalized forces of ATD.....	30
Figure 11: ATD orientation and location of impact.	35
Figure 12: Representative generalized force profiles for rigid body impact	45
Figure 13: Comparison of measured and predicted peak force magnitudes – helmeted impacts.	46
Figure 14: Measured and predicted impact location by orientation of helmeted impacts.	47
Figure 15: Comparison of measured and predicted peak force magnitudes – unprotected.	48
Figure 16: Measured and predicted impact location by orientation of unprotected impacts.....	49
Figure 17: Rigid link manipulator model, coordinate system and generalized forces of ATD.....	57
Figure 18: Observations of FIR differentiator filter of angular velocity – a) Welch power spectral density b) Zero-phase response.....	60
Figure 19: Surface geometries used to define impact location points..	61
Figure 20: Constraining impact location to a coordinate of pushing contact..	62
Figure 21: Visual comparison of predicted and actual helmeted force magnitude data	63
Figure 22: Visual comparison of predicted and actual unprotected force magnitude data.....	63

LIST OF TABLES

Table 1: List of symbols.....	32
Table 2: List of equation symbols.....	33
Table 3: Coordinate location of impact for each test scenario.....	36
Table 4: Test matrix, 3 tests of each impact scenario were performed for a total of 72 impacts..	37
Table 5: Literature model parameters	39
Table 6: Spherical coordinate angles to calculate force vector components.....	40
Table 7: Average peak linear acceleration and angular acceleration of test impacts.	43
Table 8: Mass moment of inertia	44
Table 9: Model Parameter Values	45
Table 10: Comparison of predicted force characteristics to measured	51
Table 11. Comparison of Predicted Impact Characteristics to Measured Test Values	64

LIST OF ABBREVIATIONS

ATD	Anthropomorphic Testing Device
BRIC	Brain Injury Criterion
CAD	Computer Aided Design
CDC	Center for Disease Control and Prevention
CG	Center of Gravity
CSDM	Cumulative Strain Damage Measure
CTE	Chronic Traumatic Encephalopathy
ED	Emergency Department
FEA	Finite Element Analysis
GCS	Glasgow Coma Scale
HIC	Head Injury Criterion
Hybrid III	Hybrid III 50 th Percentile Male
HIT	Head Impact Telemetry
LOC	Loss of Consciousness
MMA	Mixed Martial Arts
MPS	Maximum Principal Strain
mTBI	Mild Traumatic Brain Injury
NFL	National Football League
NFLPA	National Football League Players Association
NOCSAE	National Operating Committee on Standards for Athletic Equipment
SCAT	Sport Concussion Assessment Tool
SR	Sports and Recreation
TBI	Traumatic Brain Injury

ABSTRACT

Brain injuries sustained during an impact to the head during sport and recreation related activities are a common occurrence. They can cause adverse effects in injured participants, some of which are identifiable immediately following contact, while others may not manifest for years. The study of concussive and sub-concussive impacts of sport and recreation activities is important in understanding the mechanism of impact, resultant brain response, and how injury manifests to improve risk of injury assessments, game-play decisions, and protective equipment. This study aims to relate the kinematic motion experienced by the head during impact, to the characteristics, magnitude, direction, and location, of the force applied to the head during contact. To investigate this relationship, a pendulum impact device was designed to replicate on-field impacts of contact sports, kinematic data was collected from an anthropomorphic test device during an applied impact, and the resultant kinematics were related to applied generalized force through Euler-Lagrange dynamics of a simplified rigid link model. Through this system of dynamic equations, the characteristics of applied force were predicted within reasonable bounds; the results of this study could lead to better on-field injury assessments and improved protective equipment.

INTRODUCTION

Traumatic brain injury (TBI) is a growing health concern in the United States and around the world. Caused by a sudden trauma, such as an impact to, or rapid acceleration/deceleration of, the head, TBI can cause short-term and long-lasting effects on brain function. While efforts have been made to mitigate the incidence of injury, TBI accounts for an estimated 2.5 million emergency department visits annually in the United States, for injuries related to falls, motor vehicle crashes, sports injuries, and others [1]. The most common severity of TBI that patients present with is mild traumatic brain injury (mTBI), more colloquially known as concussion [2]. While mTBI is the least severe index of TBI incurred, it is still associated with loss of consciousness (LOC), memory loss, altered mental state, and cognitive deficits [2], [3]. While an mTBI can be incurred through any number of events, a high incidence of injury comes from voluntary participation in sport and recreation activities.

Approximately 25% of adults and 75% of children (≤ 17 years of age) participate in a sport activity [4]. Recent Center for Disease Control and Prevention (CDC) data suggests that an average 283,000 emergency department (ED) visits are attributed to sports and recreation (SR) related TBIs annually [5]. Furthermore, it is estimated that up to 3.8 million SR mTBIs are incurred annually in the U.S., due to underreporting and not seeking medical care; 1.9 million of which are incurred by children under 18 years of age [6], [7], [8]. Mild TBIs are not the only concern when it comes to sports related head impacts; sub-concussive impacts, defined by Bailes et al. as “cranial impacts which do not result in diagnosed concussion,” [9] are a regular occurrence for athletes who participate in contact sports. As with any injury continued exposure to trauma, even mild trauma, will compound the effects of injury. It is suggested that prolonged exposure to repetitive head

impacts is linked to changes in neurophysiology, including neurodegeneration and chronic traumatic encephalopathy (CTE) pathology [10], [11].

Efforts have been made to reduce SR participants risk for head impact injury by mandating, prohibiting, and promoting certain protective equipment,¹ and updating rules and protocols for game-play and sport participation. While there has been some decline in SR-TBI-ED visits by children (32% over a 6-year period) [5], athletes of all ages are still at risk and incurring injury daily. The deleterious effects of SR head impacts along with the high rate of incidence within the U.S. warrants cause for concern and investigation. Understanding the mechanism of impact, associated brain response, and how injury manifests is critical to developing better risk of injury assessments, game-play decisions, and improved protective equipment.

¹ Annually the National Football League (NFL) in collaboration with the National Football League Players Association (NFLPA) publish a list of approved helmets which have been tested to determine which helmets best reduce impact severity [34]

CHAPTER 1: Head Impact Biomechanics

To begin to understand the mechanism of head trauma and the brain's response to rapid motion, researchers have captured and analyzed real world impact data, recreated impact scenarios in the laboratory, and modeled impacts to analyze the kinematics, or motion, stresses and strains that the brain experiences during an impact.

1.1 Real-World Impacts

There is an exhaustive list of the sport and recreation activities that place participants at risk of incurring head trauma. However, the most commonly studied activities are those with a large number of participants worldwide, such as soccer and bicycling, or those where the risk of contact and injury are high, such as American football, rugby, ice hockey, and combat sports (boxing, mixed martial arts (MMA), etc.). One aspect of researching sport related impacts is understanding how the head responds to contact during game-play.

1.1.1 Kinematic Data Collection

While it is possible to simulate different contact sports in the laboratory setting, the best way to analyze a participant's kinematic response to head impact is to observe live events and capture data on how the participants react to game-play contact. Two of the most common sensors used to capture kinematic data are the accelerometer, which collects acceleration data along the axis of motion, and the gyroscope, which collects angular velocity data about the axis of rotational motion; combining these two types of sensors yields an object's inertial response to motion. Now, able to be manufactured on a millimeter scale, along with wireless technology, these sensors can be integrated into sport equipment or directly fixed to the participant.

A common equipment integrated sensor is the Head Impact Telemetry (HIT) System (Simbex, Lebanon, NH). This system captures acceleration of the head via six accelerometers

mounted within a helmet [12]. The HIT systems have been integrated into ice hockey and American football helmets to evaluate the acceleration of players' heads following contact in their respective sports. Skin patches imbedded with inertial sensors are another method for collecting head motion data from sport participants. Sensors such as the xPatch (X2Biosystems, Inc.) can be attached to the skin over the mastoid process, or just under the ear, in close proximity to the head's CG. While used to collect a large amount of impact data, these two data collection systems have their pitfalls; helmets can be worn improperly and move independently of the head [13], and skin patches are subject to soft tissue movement [14]. Sensors would be less prone to noise if they could be rigidly fixed to the participant, such as holding the sensor between the participant's jaw.

Instrumented bite bars and mouthguards have been shown to have tight coupling to the skull when collecting data from low-level soccer head impacts when compared to the other wearable impact sensors [14]. Mouthguards, a piece of protective equipment that is required, or encouraged for the most common types of contact sports, are an ideal vehicle for inertial sensors; they bridge the gap between being integrated to equipment and directly to the participant. The use of instrumented mouthguards in contact sports is providing a realistic look into the kinematic motion of the head during impact.

1.1.2 Video Analysis

While instrumenting sport participants directly is the best way to gain insight into kinematic motion of the head, it does not always tell the whole story about head impacts; such as, where the player was hit, or what the closing velocity of two players was. The opportunity presents itself to analyze these aspects of contact sports when video data is available. Some researchers rely on recording their own head impact videos while others consult footage captured during broadcast sporting events, the analysis process for each scenario is the same. The video recordings are

reviewed and impacts which meet a predetermined criteria are selected. These events are then analyzed further to determine the orientation of the players involved in the impact, closing velocities, and in some cases the type of helmet worn by the participants [15]. Knowing the initial characteristics of the real-world impact allows researchers to recreate the impact scenario in the laboratory.

1.2 Impact Recreation

Evaluating head impacts in the laboratory enables researchers to conduct data collection and analysis without putting sport participants at further risk of injury. To capture consistent, reliable results, it is possible to rigidly fix sensors to a representative head, repeat multiple impacts, and control variables such as the orientation of the head or impact energy when conducting impact testing in the laboratory. While different methods, devices, and targets are used during laboratory head impact recreations, the end goal is the same: to better understand how the head behaves during a representative impact.

After analyzing the initial characteristics of an on-field impact researchers recreate the impacts in the laboratory with cadaver models or an anthropomorphic test device (ATD). Many cadaver studies are focused on soft tissue motion and the displacement of the brain throughout impact. Hardy et al. [16], [17] used high-speed biplane x-ray and neutral density targets to conclude that the brain is displaced relative to the skull during impact, and furthermore, that regions of the brain closer to the center of gravity (CG) of the head are displaced less than regions further away from the CG.

ATDs are designed to mimic the human body in physical attributes (mass, dimension, density, etc.); and while not fully biofidelic they are not subject to degradation and can give insight into the kinematics experienced by the head during impact. In a study of American football

concussive helmet-to-helmet impacts Funk et al. [15] reconstructed on-the-field impacts to capture the biomechanical parameters and kinematic response of the body through the impacts. Results from both avenues of impact reconstruction can then be used to define simulation models or thresholds to quantify and assess a participant's risk of injury.

1.3 Injury Analysis

As discussed in the Introduction, some traumatic brain injury events can be diagnosed by physical symptoms exhibited by the injured participant. However, each participant will not respond to injury the same way, or exhibit the exact same symptoms; especially when it comes to mild impacts or repetitive exposure. Physical symptoms of brain injury are a qualitative assessment generally assigned to a quantitative scale, such as the sport concussion assessment tool (SCAT) or the Glasgow coma scale (GCS). SCAT is a score card where physical symptoms such as vision problems, fatigue, or balance are rated on severity to assess a player's condition after concussion [18]. The GCS is an assessment of consciousness for more severe TBI and relies on quantifying a patient's response to ocular, verbal, and motor stimulation [19]. While these qualitative assessments are good for patients presenting with injury, they do not define a quantitative threshold for the extent of injury; this is where researchers have used real-world data and results from laboratory recreations to quantitatively assess injury through metrics and finite element analysis.

1.3.1 Injury Metrics

Quantitative injury metrics are often defined by building mathematical models from the kinematic response of the head. One of the most widely used metrics is the head injury criterion (HIC) which uses linear acceleration of the head to assess the likely hood of head injury in the event of an impact, the criteria thresholds are defined for car crash scenarios [20]. Held as the standard for defining car safety, HIC does not account for the rotational motion of the head. This

diffuse axonal injury, or shearing of the brain tissue during rotation, makes a large contribution to the overall extent of injury for TBI patients [21]. To incorporate rotational motion into a risk of injury metric the brain injury criterion (BRIC) was developed; BRIC is the ratio of max angular velocity and angular acceleration experienced by the head compared to critical values of angular velocity and acceleration determined by finite element testing [22]. Many other metrics have been developed with the common goal of using resultant kinematic motion of the head to attempt to define thresholds and risks of injury. Often these thresholds are defined from the stresses and strains experience by the brain during rapid movement simulated by finite element models.

1.3.2 Finite Element Analysis

Finite element analysis (FEA) is used to numerically solve complex problems in solid mechanics [23]. Seen as a deformable body, the head and brain are modeled with physical characteristics informed by human cadaver testing. The models then rely on numerical computation of mechanics principles to quantify deformation of the brain; some of the tissue level metrics used to evaluate deformation include maximum principal strain (MPS), Von Mises stress, pressure, cumulative strain damage measure (CSDM), and axonal strain [24]. MPS, the peak strain experienced by the region of interest, and CSDM, a measure of the cumulative regions of the brain experiencing strain over a certain threshold [25], are common metrics used in head impact FEA. The inputs to the head FEA models are often the resultant kinematics from head motion and the results of FEA give insight into the amount of strain, or deformation, the brain experienced during the impact. It is expected that the FEA models will behave similarly to cadaver testing. As seen in [16], peak maximum principal strain and maximum shear strain in cadaver testing increase as linear acceleration of the head in the direction of impact increases; FEA models of the head should behave similarly.

Increases in kinematic response of the brain have been correlated to higher levels of strain and deformation of the brain predicted by FEA models, which have been correlated to severity of injury. Angular velocity has shown to have a direct correlation with CSDM [26]; furthermore, in [27] it was observed that in loss of consciousness head impacts the resultant tissue-level strains were nearly 50% higher than average non-injury results. These findings show that increasing the energy of impact, increases the head's kinematic response, which leads to higher predicted strain and increased risk of injury. To expand on these areas of research, Elkin et al. [28] related brain strain to location of impact; from their study of ATD impacts they found that "... the magnitude and regional distribution of brain strain is a function of impact energy and impact location on the football helmet." Revealing that the amount of brain strain, and risk of injury, is not solely driven by the force of impact, but also by what region of the head was impacted.

1.4 Research Focus

While substantial strides have been made in impact biomechanics, there are still open research questions that need to be addressed. For determining initial impact conditions, researchers currently rely on video or word of mouth; however, not all impacts are recorded, video is not always clear, and witnesses may not be available. Kinematics acquired from instrumented players are reliable in capturing the motion of the head, FEA can be a time-consuming process, and injury metrics do not account for initial impact characteristics, nor do they consider the location of impact. To better understand the mechanism of impact, inform return-to-play decisions, and develop better protective equipment the gap between kinematics and impact characteristics needs to be bridged; this can be done through dynamic analysis of the impact scenario. The focus of this research is to replicate impact conditions of contact sports, within a known coordinate reference, to predict location, direction and magnitude of impact force based on measured kinematics.

CHAPTER 2: Impact Device

2.1 Background

Recreating head impacts in the lab requires a means of applying force to a representative head; however, the application of force must be controlled, consistent, and conducted in a safe environment. Viable impact devices include the drop tower, linear impactor, and pendulum. The drop tower relies on the weight of the ATD and gravity to apply the force of impact; it is generally associated with the standards for bicycle helmet testing [29]. However, there are few ways to adjust the energy of impact, and the orientation of the ATD during the drop test limits rotation of the head. Linear impactors allow the user to apply variable force with limited adjustments to the test set-up; often designed with a pneumatic ram, changing the charged pressure can produce a range of impact velocities [30]. Unfortunately, linear impactor systems are often costly; a more cost-effective means to apply force would be to build the impact device in-house.

For this study, a pendulum impactor was designed to replicate on-field head impacts. The pendulum has been used in a variety of impact applications, relies on a simple design, and has been an integral part of helmet testing, particularly American Football helmet testing [31]. By using a pendulum, the ATD can remain stationary, or fixed on a target table, and the energy of impact can be varied by adjusting the height from which the pendulum is dropped, and/or by modifying the mass of the impactor. By keeping a record of impact mass and drop height, impact energy can be repeated with confidence; lending a method that is versatile, repeatable, and safe to use.

2.2 Impact Device Design

2.2.1 Design Considerations

To establish a unique perspective on impact testing, design considerations were made to provide robust impact characteristics through a variable weight end mass, ensure ease of access

and installation through a separable frame, and guarantee safety of operators through material stress analysis. Each space is unique, and with each iteration of component design improvements should be made to ensure compatibility with research goals and available resources. The design for this study's pendulum was referenced from the specifications of Virginia Polytechnic Institute's Hockey STAR pendulum [32]; the height, end mass, and materials were used as a template to begin the design process. However, due to available laboratory space and location, material and equipment availability, as well as research objectives, changes were made to the Hockey STAR design to accommodate the laboratory's needs. These considerations were made to create a more robust impact system, enabling modification of the pendulum to fine tune impact parameters on a system that could be used for future research applications. Assembly drawings and bill of materials for the pendulum can be found in Appendix I. Figure 1, is a SOLIDWORKS rendering of the complete pendulum assembly.



Figure 1: SOLIDWORKS® rendering of the complete pendulum design.

2.2.2 Force Analysis

To ensure that testing is completed in a safe environment with reliable equipment force and moment analysis was completed for the different components of the impact device.

2.2.2.1 Variable Impact Mass

To adequately represent the gamut of head impact conditions that a human head may experience, the impact magnitude during recreations needs to be variable. Beyond just adjusting the drop height of the pendulum arm to control impact velocity, an end mass of separate, removable steel plates was designed to change the impact mass. This allows for greater control over the impact energy as designing a larger apparatus, to extend the length of the lever arm and increase impact velocity, would lead to difficulties in fabrication and installation. Thus, low energy impacts can be created with a smaller impact mass dropped from a low angle, and high energy impact tests completed with larger angles and greater mass.

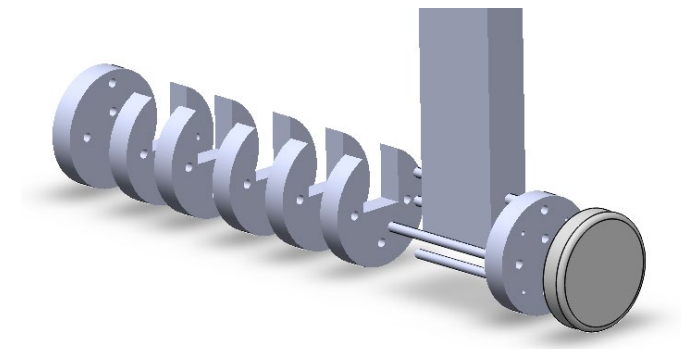


Figure 2: Variable mass and end cap for pendulum arm.

A design was established which utilizes threaded rods and 1-inch steel plates to create an impact mass which can be modified to suit a variety of impact conditions. In total there are 7 steel plates; 1 is fitted with 5 tapped holes to accommodate 3/8” threaded rods to fix the impacting mass to the pendulum arm and to attach the other 6 steel plates. Figure 2, is the SOLIDWORKS

rendering of the pendulum end-mass. Two of the threaded rods are used to fix the end-mass to the end of the pendulum arm to prevent movement or rotation of the end-mass during impact. All the threaded rods are capped with nuts and lock washers to ensure a secure hold during impact testing.

A nylon endcap, to protect the ATD, is attached to the main steel plate via a load cell to capture force data; though the load cell can be removed, and the endcap can be fitted using the threaded rods. Fitted with all 7 steel plates the largest impact mass is 15.3 kg; utilizing only the endcap and the main steel plate, the impact mass is 2.9 kg. The end-mass of the impactor was an important factor to consider in evaluating the forces and moments that the frame, pendulum arm, and pivoting rod undergo during testing.

2.2.2.2 Frame

The frame was designed using 2-inch square, 0.25-inch-thick steel tubing. This material offers strength and durability, without being overly bulky. The frame was designed to be assembled/disassembled with nut and bolt connections. This allowed for ease of transportation of the frame and final assembly in the designated space. Truss structures were added for additional support and a shock absorber was mounted on a cross beam to decelerate the pendulum arm after impact. For final assembly the frame was set on rubber discs to dampen vibration and fixed to the floor using concrete anchors to ensure secure placement of the pendulum apparatus.

2.2.2.3 Pendulum Arm

The pendulum arm is designed to rotate freely and deliver the impact to the ATD; to ensure durability and strength, without adding excess weight, the material selection for the pendulum arm was 6061 aluminum tubing. The main section of the arm is 190.5 cm (75 inches) from the center of rotation to the center of impact and is constructed from 2 x 4 inch, ¼ inch thick rectangular aluminum tubing. Two supports of the same material frame either side of the main section of the

arm, and all three are welded to an aluminum tube (3.5-inch outer diameter, 3-inch inner diameter) into a truss structure. Along with the pivot rod, two insert bearings are inset on either side of the aluminum tub.

2.2.2.4 Pivot Rod

Consideration was given to selecting point of rotation for the pendulum arm. At the highest drop angles, with the greatest impact mass, the point of rotation could see over 1000 Newtons of force; although distributed over the length of the support section of the pendulum arm, the worst-case scenario would be all the force concentrated at the center of the rotation point. A high strength 4140 steel alloy rod of $\frac{3}{4}$ " diameter was selected to act as the point of rotation for the pendulum. The pivot rod is fixed to the top sides of the frame using bolted U-clamps, the insert bearings connecting the pivot rod to the pendulum arm ensure smooth rotation and friction reduction as the pendulum arm swings.

2.2.6 Pendulum Control

An impact pendulum is poorly designed if it is difficult to raise and drop the pendulum arm. To safely raise the pendulum a remote-controlled wench was rigidly attached to the ceiling above the CG of the pendulum arm at full 90° extension. To safely release the pendulum an electromagnet was wired to a toggle switch; a steel plate was bolted to the pendulum arm as a ferrous material for the electromagnet to attach to.

2.3 Anthropomorphic Testing Device (ATD)

The purpose of building the impacting device was to simulate on-the-field impacts in a laboratory setting. To best represent those real-world impacts, applied force needs to mimic real-world forces, and they need to be applied to the best representation of the human head. This means

using a representative head, neck, and torso which can move and adapt similarly to the human body.

2.3.1 Biokinetics Target Table

When an object is met with a force, if it is unconstrained, it will move in the direction force was applied; on the field when a player receive an impact to the head, his head and body will respond to that impact and move in the direction force was applied. To recreate this scenario in the lab we used a target table (Biokinetics and Associates Ltd. Ottawa, Canada). The target table is used to orient the head form (target) and allow for translation of the head along the direction of impact. The target table is adjustable in three translations (fore/aft, vertical, and lateral) and has a mount which can be tilted and twisted – allowing for 5-axis transformation of the target. The target mount sits on a rail system which allows for translation of the target when force is applied.

2.3.2 Hybrid III Neck

The Biokinetics target table has been specifically designed to accommodate the Hybrid III (HIII) 50th percentile male neck (Humanetics Farmington Hills, MI). Designed for car crash testing, the HIII 50th male dummy is the most widely used ATD body form available. Figure 3, it the HIII neck form fitted with the NOCSAE head form.



Figure 3: NOCSAE head form on Hybrid III neck

2.3.3 NOCSAE Head Form

The National Operating Committee on Standards for Athletic Equipment (NOCSAE) is an organization focused on reducing injury in sports. Researchers developed the NOCSAE head form for football impacts. While there is a HIII 50th head, the NOCSAE head form has been shown to have a better fit to American football helmets and is representative of physical features of the human head [33].

2.3.3.1 Custom Head-Neck Attachment



Figure 4: Custom head-neck attachment

The NOCSAE head form and HIII neck are not directly compatible to attach to one another, so it was necessary to design an assembly of parts to create a connection joint. To represent the craniovertebral junction, a pin joint for minimal fore/aft (nodding) rotation with rubber dampers was chosen as the connection type. An aluminum plate to match the HIII neck was designed with inset pads for rubber dampers and a pin slot extruded from the center. An aluminum block with a threaded bolt to attach to the NOCSAE head form and inset holes for the pin completed the second part of the connection.

2.3.3.2 *Helmet*

American football is one of the most addressed contact sports when it comes to head injury, so it was necessary to test using a helmet and one that is commonly worn in the NFL. A new Riddell Speed helmet (Riddell Rosemont, IL) was used for the helmeted impact testing. Riddell helmets are commonly worn in the NFL and the Riddell Speed is featured on the NFL helmet testing poster results with good performance [34].



Figure 5: Assembled impact test device.

2.4 Data Collection

The purpose of this research was to relate the kinematic motion of the head during impact to the force applied to the head; to capture this information the head was fitted with a 6 degree of freedom motion sensor to capture kinematic data, the impactor fitted with a force sensor, and high-speed video was taken to capture and analyze the impact.

2.4.1 Kinematic Data

The NOCSAE head form has a channel that opens at the base of the jaw and extends up into the head form cavity. At the base of this channel there are tapped holes which can accommodate a sensor mount positioned near the head form's CG. This sensor mount was machined from a CADEX drawing for a DTS 6DX Pro (Diversified Technical Systems Inc., Seal Beach, CA) which was acquired to capture linear acceleration and rotational velocity. The 6DX Pro captures triaxial accelerometer data up to 500 g and triaxial angular velocity up to 18000 deg/s.

a)



b)

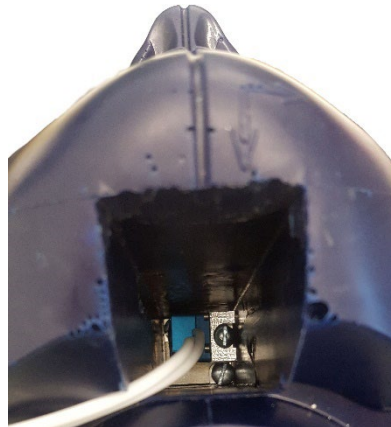


Figure 6: a) DTS 6DX Pro on custom mount

b) 6DX Pro mounted inside NOCSAE Head (bottom view)

2.4.2 Force Data



Figure 7: Load cell placement on impactor between endcap and steel plates.

Measuring the force of impact was done by fitting a compression load cell between the nylon cap and the first steel plate of the pendulum end-mass (Figure 7); the cap provided larger surface area for the point of impact and sandwiched the compression cell for accurate readings. A DYMH-103 load cell (ATO, Diamond Bar, CA) with a maximum load of 500 kg was selected for testing. It was wired for compression testing and is fixed to the end cap and steel plates by M8 threaded attachment points.

2.4.3 High-Speed Video



Figure 8: Overlay of high-speed video stills to capture the motion of the head throughout impact

High-speed video was captured using a Chronos 1.4 (Kron Technologies, Burnaby, BC, Canada) to capture head movement during impact. Slow motion play back of the video enabled analysis of the point of impact and how the head responded and moved throughout the impact.

2.4.4 Data Acquisition

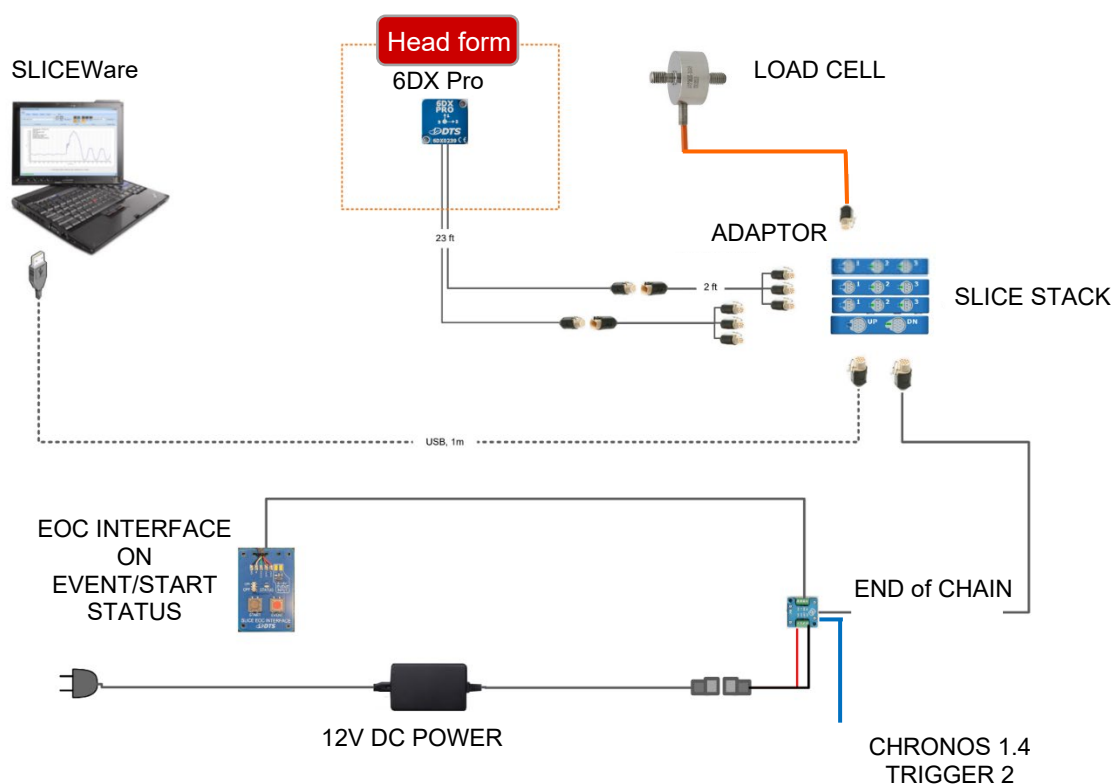


Figure 9: Data acquisition setup using DTS SLICEWare and SLICE Micro Stacks

Each piece of information collected is valuable, but when acquired synchronously it provides a full picture of the force of impact transferred to the head and how the head moves in response to the impact. A DTS data acquisition package was used for data collection. Figure 9, is a schematic of the data acquisition set up used for data collection. The 6 channels from the 6DX Pro were already compatible with the DTS package, however, the load cell had to be connected to a male end connector with proper pin placement to fit with the DTS system. DTS SLICEWare was used to record, review, and export the kinematic and load cell data for analysis. To synchronize data collection, all sensors and the high-speed camera were triggered by a step signal through the data acquisition setup; 4 seconds of data were captured after trigger for each impact.

CHAPTER 3: Mathematical Model

The head and neck of the ATD is modeled as acting as a rigid link manipulator, a series of links connected by joints; for an n degree of freedom manipulator there are n links and n joints [35]. In [36] the human head and neck was modeled as a 3 degree of freedom, 2 pivot model, to study the motion of the head and its inertial response to force; however, the motion of study was only within 1 plane of motion. For this study, a similar approach was taken in defining the head and neck through a series of links and joints, however, it was a research objective to define the model for 6 degrees of freedom.

3.1 Rigid Link Model

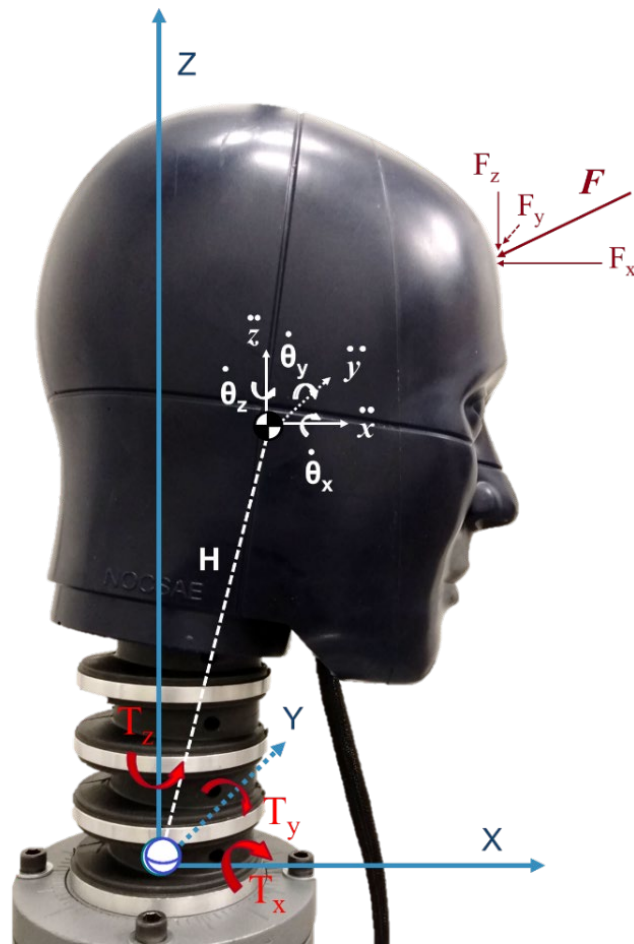


Figure 10: Rigid link manipulator model, coordinate system and generalized forces of ATD.

To capture 6 degrees of freedom, 3 linear translations along each axis, and 3 rotations about each axis, of a global Cartesian coordinate system, the ATD is modeled as a single joint between the C7 vertebra and the head CG, with a spherical joint at the base of the link. Figure 10, is a visual representation of the rigid link model defined for dynamic analysis. As previously mentioned, a rigid link manipulator generally has n joints for n links and n degrees of freedom; for this model the links and joints are defined as being coincident to one another. The length of this link is defined in the model as, H , the distance between the spherical joint and the head's CG. The degrees of motion for this model are 3 rotations about the spherical joint, captured through angular velocity and instantaneous linear translation of the head CG along each of the 3 coordinate axes, captured by linear acceleration.

The global Cartesian coordinate for the ATD is defined at the base of the HIII neck, where it is fixed to the target table and the spherical joint of the rigid link model is positioned. The global X translates to the body's anteroposterior axis, the Y to the mediolateral axis, and the Z to the caranioclonodial axis. Figure 10, is a visual representation of the rigid link model defined for this study; the figure also incorporates the generalized forces and the defined coordinate system used to derive the system equations of motion.

3.1.1 Euler-Lagrange Dynamics

Physicists and mathematicians have developed techniques to describe the physical world using systems of equations; Lagrange, a mathematician, developed a method of defining the motion of a rigid body through the systems energy and change in position over time. The Lagrangian is defined as the difference in kinetic and potential energy of a system; in an alternate form it can be expanded to include viscous damping forces and when derived with respect to position and change in position (velocity) the system of equations equals the generalized forces

acting on the rigid body. Equation 1 is an alternate form of the Euler-Lagrange used to define the dynamic equations of motion for this model, Table 1, is a list of variables and symbols.

$$\frac{d}{dt} \left(\frac{\partial T}{\partial \dot{q}_i} \right) - \frac{\partial T}{\partial q_i} + \frac{\partial D}{\partial \dot{q}_i} + \frac{\partial U}{\partial q_i} = Q_i \quad , i = 1, 2 \dots, n \quad (1)$$

Table 1: List of symbols

Symbol	Variable	Symbol	Variable	Coordinate Reference
T	Kinetic energy	Q	Generalized forces	$F_x, F_y, F_z, \tau_x, \tau_y, \tau_z$
D	Viscous damping	q	Coordinate position	$x, y, z, \theta_x, \theta_y, \theta_z$
U	Potential energy			
t	Time			
n	Degrees of freedom			

Referring to the model shown in Figure 10, the following equations (Equations 2 - 4) for kinetic and potential energy, and viscous damping were defined. The Cartesian coordinates for x, y, z positions were transformed using spherical coordinates to capture rotational motion; detailed steps to these equations and a list of variable symbols can be found in Appendix II.

$$T = \frac{1}{2} m_h [\mathbf{V}]^2 + \frac{1}{2} [\mathbf{I}] [\boldsymbol{\omega}]^2 \quad (2)$$

$$U = m_h g z + \frac{1}{2} [\mathbf{K}] [\boldsymbol{\theta}]^2 \quad (3)$$

$$D = \frac{1}{2} [\mathbf{D}] [\boldsymbol{\omega}]^2 \quad (4)$$

Equations 5 – 10 are the final Lagrange dynamic equations (derived according to Equation 1) describing the motion of the simplified rigid link manipulator model. Table 2 lists the symbols and variables used in these equations.

$$F_x = m_h \left[\ddot{x} + H \left(\ddot{\theta}_y \cos \theta_z \cos \theta_y - \ddot{\theta}_z \sin \theta_z \sin \theta_y - \cos \theta_z \sin \theta_y (\dot{\theta}_y^2 + \dot{\theta}_z^2) - 2 \sin \theta_z \cos \theta_y (\dot{\theta}_y \dot{\theta}_z) \right) \right] \quad (5)$$

$$F_y = m_h \left[\ddot{y} + H \left(\ddot{\theta}_z \cos \theta_z \sin \theta_y + \ddot{\theta}_y \sin \theta_z \cos \theta_y - \sin \theta_z \sin \theta_y (\dot{\theta}_y^2 + \dot{\theta}_z^2) + 2 \cos \theta_z \cos \theta_y \dot{\theta}_y \dot{\theta}_z \right) \right] \quad (6)$$

$$F_z = m_h \left[\ddot{z} - g - H \left(\dot{\theta}_y^2 \cos \theta_y - \ddot{\theta}_y \sin \theta_y \right) \right] \quad (7)$$

$$\tau_x = I_x \ddot{\theta}_x + D_x \dot{\theta}_x + K_x \theta_x \quad (8)$$

$$\tau_y = I_y \ddot{\theta}_y + D_y \dot{\theta}_y + K_y \theta_y + H * m_h \left[\ddot{x} \cos \theta_z \cos \theta_y + \ddot{y} \sin \theta_z \cos \theta_y - \ddot{z} \sin \theta_y + g \sin \theta_y - \frac{\dot{\theta}_a^2 H \sin(2\theta_y)}{2} \right] \quad (9)$$

$$\tau_z = I_z \ddot{\theta}_z + D_z \dot{\theta}_z + K_z \theta_z + H * m_h \left[\ddot{y} \cos \theta_z \sin \theta_y - \ddot{x} \sin \theta_z \sin \theta_y + H \sin(2\theta_y) \dot{\theta}_z \dot{\theta}_y \right] \quad (10)$$

Table 2: List of equation symbols

Symbol	Variable	Symbol	Variable
m_h	Mass of head form	$[\ddot{\theta}_x \ \ddot{\theta}_y \ \ddot{\theta}_z]$	Angular acceleration
g	Gravity (9.81 m/s ²)	$[D_x \ D_y \ D_z]$	Damping constants
H	Link length (0.218 m)	$[K_x \ K_y \ K_z]$	Spring constants
$[x \ y \ z]$	Coordinate axis position	$[I_x \ I_y \ I_z]$	Inertia tensor
$[\ddot{x} \ \ddot{y} \ \ddot{z}]$	Linear acceleration	$[F_x \ F_y \ F_z]$	Applied force
$[\theta_x \ \theta_y \ \theta_z]$	Angular position	$[\tau_x \ \tau_y \ \tau_z]$	Applied torque
$[\dot{\theta}_x \ \dot{\theta}_y \ \dot{\theta}_z]$	Angular velocity		

The inputs to these dynamic equations are the kinematic data, angular velocity and linear acceleration, collected from the inertial sensor mounted inside of the head form, as well as, the integral and derivative of angular velocity (angular position and acceleration, respectively). When

supplemented with known constants for gravity and link length, as well as physical properties of the ATD, spring and damper constants, and mass moment of inertia, the force vector applied to the head can be solved. This force vector defines two of the three impact characteristics, force magnitude and direction.

3.1.2 Moment Cross Products

To fully define the impact characteristics of a force applied to the head, it is necessary to know not just the magnitude and direction of force, but also the location of impact on the head. The final step for solving for the location of impact is to relate force to torque; this relationship is analogous to solving for a force moment, which is found by taking the cross product of the lever arm with the applied force (Equation 11).

$$\mathbf{M} = \mathbf{r} \times \mathbf{F} = \begin{vmatrix} \mathbf{i} & \mathbf{j} & \mathbf{k} \\ r_x & r_y & r_z \\ F_x & F_y & F_z \end{vmatrix} \quad (11)$$

Using this same relationship, the force components calculated by the dynamic equations can be related to torque with the coordinate location of impact. Equations 12 – 14 are used to solve the unknown \mathbf{R} , or coordinate location of impact from force and torque calculated from the dynamic equations.

$$\tau_x = R_y F_z - R_z F_y \quad (12)$$

$$\tau_y = R_x F_z - R_z F_x \quad (13)$$

$$\tau_z = R_x F_y - R_y F_x \quad (14)$$

Through these 9 relations derived from Lagrange dynamics of the simplified rigid link model (Equations 5-10 and 12-14) the force characteristics, magnitude, direction, and location of impact can be defined from kinematic motion data captured from the head's response to impact

CHAPTER 4: Experimental Methods

4.1 Test Matrix

To capture a range of impact conditions testing was conducted for 2 sport conditions, on 4 locations of the head, with 3 categories of impact force.

4.1.1 Sport Selection

The two sport conditions chosen for impact recreation were American football and unprotected combat sports, such as MMA or boxing. American football is often the focus of head impact and traumatic brain injury studies due to media coverage, and popularity, of the NFL, as well as the large number of youth and collegiate participants throughout the United States. To contrast American football where players are required to wear protective equipment, combat sports were selected due to the lack of protective head gear and high incidence of head impacts².

4.1.2 Impact Locations



Figure 11: ATD orientation and location of impact.

The four impact locations chosen for testing were the frontal, right oblique, parietal, and occipital regions of the skull (Figure 11). These regions are common contact locations for football players, [37], [38] and also encompass common regions of contact from MMA and boxing data

² 52% of male heavyweight MMA matches end in head trauma; in MMA this is a knockout or technical knockout [52].

[39]. Only the right parietal and right oblique regions were chosen as test locations as it is assumed that the kinematic response of the head would be mirrored for contact to the left parietal and oblique regions. Frontal and occipital regions were chosen for their frequency of contact during the chosen sports as well as the difference in physical properties that the ATD exhibits for either positive or negative rotation about the global Y axis (mediolateral axis). The HIII neck has been designed to replicate the human neck's response to impact and therefore exhibits different spring and damper behavior when force is applied to the front, versus the back, occipital region. Figure 11, is a visual representation of the orientations of the head and the location of impact, the force applied by the pendulum is represented by the red arrow. Similar orientation and location of impact were used for the unprotected ATD tests, the global coordinate location for each impact by orientation is listed in Table 3.

Table 3: Coordinate location of impact for each test scenario, Cartesian and spherical coordinates. *H* denotes helmeted, *U*, unprotected.

Location Condition		Frontal		Right Oblique		Parietal		Occipital	
		H	U	H	U	H	U	H	U
Distance (cm)	x	20.6	11.2	15.2	7.5	2.2	0	-11.2	-7.6
	y	0	0	-8.7	-6.3	-11.9	-6.9	0	0
	z	26.8	29.3	28.2	29.8	27.9	30.7	27.6	23.9
	$\ \mathbf{R}\ $	33.8	31.4	33.2	31.4	30.5	31.5	29.5	25.1
Angle (°)*	α	0	0	-30	-40	-80	-90	180	180
	β	37.98	20.9	31.9	18.2	23.31	12.7	22.5	17.64

*Spherical coordinate angles, not adjustment angles for ATD and target table

4.1.3 Impact Categories

Force level categories of high, mid, and low were selected to group the force readings observed by the load cell at different pendulum mass and drop heights. High force readings were observed during initial testing of unprotected test conditions at a drop height of 10°; however, there was little variation between orientations. The threshold limit for the load cell used to collect force readings was 500 kg. Therefore, testing was completed at relatively low drop angles for

unprotected scenarios with an impacting mass of 10.4 kg; each orientation was impacted from the same drop angles 5°, 10°, and 18° to represent low, mid, and high levels of impact, respectively.

Helmeted test conditions allowed for higher pendulum mass and drop angles; however, due to the helmet's design each orientation saw different peak force readings at the same mass and drop angle. An end-mass of 15.3 kg was used for helmeted testing. To remain within the service limits of the load cell the impact categories were grouped by the unfiltered load cell readings collected during preliminary testing. Readings of approximately 250 kg, 350 kg, and 450 kg were set as the target for the low, mid, and high levels of impact, respectively; the drop angle varied for frontal impacts. Higher drop angles were required to meet the category thresholds, this could be attributed to the design of the helmet to mitigate the force from the most common contact location. Table 4, outlines the drop angles chosen for each impact category. Post processing the average force readings for each category were 201.3 kg, 297.5 kg, and 400.6 kg. While higher drop angles would yield higher kinematic response, closer to concussive level metrics, maintaining the integrity of the load cell was prioritized.

Table 4: Test matrix, 3 tests of each impact scenario were performed for a total of 72 impacts.

Helmeted			Unprotected		
15.3 kg impacting mass			10.4 kg impacting mass		
Orientation	Impact Category	Drop Angle(°)	Orientation	Impact Category	Drop Angle (°)
Frontal	Low	40	Frontal	Low	5
	Mid	60		Mid	10
	High	75		High	18
Right Oblique	Low	30	Right Oblique	Low	5
	Mid	40		Mid	10
	High	60		High	18
Parietal	Low	30	Parietal	Low	5
	Mid	40		Mid	10
	High	60		High	18
Occipital	Low	30	Occipital	Low	5
	Mid	40		Mid	10
	High	60		High	18

4.2 Signal Processing

Kinematic data from the 6DXPro mounted in the head form serve as the inputs to the dynamic equations and the force readings from the load cell are the ground truth measurements to which the predictions are compared. All 6 channels of kinematics, 3 angular velocity, 3 linear acceleration, and 1 channel for the load cell reading were recorded via DTS SLICEWare at 20,000 Hz. The raw, unfiltered data was downloaded via .CSV files and imported for post processing. The time series kinematic data was filtered using a fourth-order Butterworth filter with cutoff frequencies of 300 Hz for accelerometer and load cell data, and 184 Hz for gyroscope data. All data was trimmed to a region of interest surrounding the time of the peak force reading; 3.5 milliseconds before and 11 milliseconds after for unprotected impacts and 7.5 milliseconds before and 22.5 milliseconds after for helmeted impacts.

Angular position and angular acceleration are also necessary inputs into the rigid link dynamic equations. Angular position was acquired simply by applying MATLAB's (Mathworks, Waltham, MA) cumulative trapezoidal integration to each component of angular velocity. A finite impulse response (FIR) filter was designed to take the derivative of angular velocity to acquire angular acceleration. A 250th order FIR filter with a bandpass frequency of 1000 Hz and stop pass of 1200 Hz was designed for the differentiator. Representative Welch power spectral density and zero-phase response plots can be found in Appendix III. These kinematic signals, linear acceleration, and angular position, velocity and acceleration are the inputs to the dynamic equations to solve for the generalized forces on the test system.

4.3 Model Parameters

The last step in fully defining the dynamic equations is fitting values to the model parameters; the dynamic equations rely on constants for mass moment of inertia, I , stiffness (spring constant), K , and viscous damping constant, D . Table 5, lists some of the model parameters that have been investigated throughout literature. However, the impact conditions of the previous studies do not completely align with the methods and objects of this current study. In this study, the HIII neck is rigidly fixed, and only part of the neck rotates with applied force which could influence the parameter values. For this study the model parameters of the ATD were fit to the experimental data.

Table 5: Literature model parameters

Component	Moment of Inertia ($\text{kg} \cdot \text{cm}^2$)			Dynamics Stiffness ($\frac{\text{N}\cdot\text{m}}{\text{rad}}$)			Damping Factor
	I_x	I_y	I_z	Flexion	Extension	Lateral bending	
NOCSAE Head Form [40]	183	167	240				
HIII Neck [41]	28.7	9.49	29.04	258.7	108.3	238.6	0.2
Riddell Speed Helmet [40]	203	255	267				

The dynamic equations for torque (Equations 8 - 10) rely on the values of the ATD physical parameters of mass moment of inertia, stiffness, and damping, to find the best value of fit for these terms simplified testing was conducted on the ATD and the coefficients of the dynamic torque equations were fit to the measured ground truth torque values. The simplified test consisted of fixing the slide table, to reduce translation of the head form and impacting the head at the four impact locations. Ground truth measurement was calculated using the equations for torque (Equations 12 - 14) with inputs being the force readings from the load cell and measured location of impact. The force from the load cell was resolved into coordinate components using spherical

coordinate angles, shown in Table 6; the distance (R_x, R_y, R_z) values are a function of time and are defined to change with angular position.

Parietal test impacts were used to fit model properties about the global X, anteroposterior axis, while right oblique impacts were used to fit model properties about the global Z, craniocaudal axis. Both occipital and frontal impacts were used to fit properties about the global Y, mediolateral axis; occipital impacts for flexion (positive rotation about Y axis) stiffness and damping constants, and frontal impacts for extension (negative rotation about Y axis) stiffness and damping constants. Mass moment of inertia about the Y axis was fit using frontal impact data and used in final results calculation for all orientations. Three impacts were completed per impact category per orientation on the unprotected ATD, for nine samples per fit.

All nine test impacts, per orientation, were fit to their corresponding ground truth value consecutively using MATLAB's "fmincon" function with literature values as initial guesses, to find the minimum of the constrained multi variable function. Mass moment of inertia terms were bound between 0 and 1 ($\text{kg}\cdot\text{m}^2$), stiffness between 0 and 1000 ($\frac{\text{N}\cdot\text{m}}{\text{rad}}$) and damping between 0 and 30 ($\frac{\text{N}\cdot\text{m}\cdot\text{s}}{\text{rad}}$) [36]. The root mean squared error (RMSE) between the dynamic torque equations and the ground truth torque values was calculated and the minimum RMSE across the data set was selected. The corresponding coefficients for mass moment of inertia, and spring and damping constants were selected for use in final dynamic equation calculations.

Table 6: Spherical coordinate angles to calculate force vector components

	Orientation	Frontal		Right Oblique		Parietal		Occipital	
	Condition	H	U	H	U	H	U	H	U
Spherical	α	0	0	130	100	90	90	0	0
Angle ($^\circ$)	β	270	270	115	100	105	105	90	90

4.4 Predicting Impact Location

With the rigid link model dynamic equations and model parameters fully defined, the last step is to relate the predicted force vectors to the calculated torque to determine the predicted impact location on the head form. A shell of all possible impact points was created by importing STL geometries into MATLAB and creating an array of the x, y, z coordinates of each point. The surface geometry for unprotected ATD conditions was defined by importing NOCSAE head form dimensions into SOLIDWORKS (Dassault Systèmes, Waltham, MA) and generating a representative 3-dimensional model mesh to export. An open-source Riddell helmet geometry was used to define the helmeted condition surface geometry [42].

The array location of peak predicted force magnitude was determined and the corresponding force vector components (Equations 5-7) were solved at that location. The predicted force components were selected as inputs to solve the linear system of torque equations (Equation 15). The ATD geometry coordinate array was the \mathbf{R} distance inputs to the linear system of torque equations.

$$\begin{bmatrix} 0 & F_z & -F_y \\ -F_z & 0 & F_x \\ F_y & -F_x & 0 \end{bmatrix} \begin{bmatrix} R_x \\ R_y \\ R_z \end{bmatrix} = \begin{bmatrix} \tau_x \\ \tau_y \\ \tau_z \end{bmatrix} \quad (15)$$

Cosine similarity (Equation 16) was determined between the predicted torque ($\boldsymbol{\tau}_p$), and the calculated torque from the system of dynamic equations (Equations 8-10) which serve as the ground truth ($\boldsymbol{\tau}_c$). A cosine similarity, φ , of 1 indicates the vectors are parallel in the same direction, 0 the vectors are orthogonal, and -1 the vectors are opposite of one another. A cosine similarity nearest to 1 is the ideal case.

$$\cos \varphi = \frac{\boldsymbol{\tau}_c \cdot \boldsymbol{\tau}_p}{\|\boldsymbol{\tau}_c\| \|\boldsymbol{\tau}_p\|} \quad (16)$$

The ATD geometry array was then sorted in descending order by cosine similarity and cut off at a threshold of 10^{-5} less than the maximum cosine similarity. This shortened array of possible impact coordinates then endured a series of logic gates to remove impact locations that result in a pulling force.³ Leaving a final array of the most likely points of impact on the ATD surface geometry; the Euclidian distance between the corresponding predicted torque values and the calculated torque values was found. The predicted point with the smallest Euclidean distance between predicted torque to calculated torque was selected as the point of impact. Figures of ATD surface geometries and detailed steps to defining impact location can be found in Appendix III.

³ Imagine a ball fixed on a stick, pushing on the ball's right side will result in rotation to the left, the same rotation can be achieved by pulling on the ball's left side. Since the area of study is impacts, the contact point for the pushing force is desired.

CHAPTER 5: Results

5.1 Kinematic Measurements

The force of impact applied to the ATD during testing resulted in kinematics consistent with average sub-concussive peak linear acceleration (PLA) and peak angular acceleration (PAA) values from literature. The average sub-concussive head impact rotational acceleration of 335 collegiate football players was 1230 rad/s^2 and the average concussive rotational acceleration was 5022 rad/s^2 [43]. Rowson *et al.*, [32] suggests that for frontal impacts PAA of the head, 3646 rad/s^2 , falls beneath the concussion average. For unprotected combat sports PAA ranges from $1704 - 2248 \text{ rad/s}^2$, with PLA averaging between $17.7 - 19.3g$ [39]; however, MMA contacts have recorded PLA up to $86.7g$ [44].

Table 7, outlines the average peak linear and angular accelerations for the varying test case scenarios. Both helmeted and unprotected ATD conditions resulted in PLAs over $60g$ and PAAs over 4000 rad/s^2 , fitting below literature averages for concussive impacts, however; the results do coincide with average sub-concussive impact kinematics. Incorporating a load cell with a higher force threshold would allow for higher energy impacts and push impacts into the concussive range.

Table 7: Average peak linear acceleration and angular acceleration of test impacts.

Condition	Impact Category	PLA (g)	PAA (rad/s^2)
Helmeted	Low	38.2 ± 5.95	2358.2 ± 1165.4
	Mid	55.1 ± 8.24	3095.2 ± 144.9
	High	84.6 ± 11.2	4166.2 ± 2113.1
	All Levels	59.3 ± 21.2	3206.6 ± 1747.3
Unprotected	Low	30.9 ± 7.85	1863.0 ± 900.9
	Mid	60.1 ± 6.84	3598.5 ± 1147.4
	High	80.7 ± 3.66	4616.9 ± 1200.4
	All Levels	57.1 ± 21.6	3359.5 ± 1565.6

5.2 Model Parameters

Mass moment of inertia, torsional spring constant, and viscous damping constant were fit experimentally using test data and derived Lagrange equations by minimizing RMSE. During post-processing and data analysis, final corrections were made to mass moment of inertia terms to best fit the experimental data (Table 8). Unprotected right oblique impacts required a higher value of mass moment of inertia about the anteroposterior axis (I_x) to fit to experimental data. This could be contributed to the physical properties of the HIII neck, and that angular motion is not directed about a single coordinate axis; the impact to the right oblique portion of the head form results in rotation about all three coordinate axes.

Table 8: Mass moment of inertia

Impact Condition	Mass moment of inertia (kg·m ²)		
	I_x	I_y	I_z
Helmeted	0.24	0.16	0.04
Unprotected	0.24	0.18	0.05
Unprotected Rt. Oblique	0.6	0.18	0.05

The spring and viscous damping constants were fit experimentally from testing conducted with fixed translation, only allowing for rotation about the HIII neck. Table 9 outlines the spring and damping constants about each axis. Torque about the mediolateral axis (τ_y) requires different spring and viscous damping constants dependent on if the force is applied in the -x, toward the front, or +x, toward the back of the head due to the HIII neck having different physical properties for extension and flexion. Therefore, occipital impacts were fitted with different spring and viscous damping constants about the mediolateral axis (K_y , D_y) for neck flexion, lowering head to chest.

All other orientations (right oblique, parietal, and frontal) use spring and viscous damping constants fitted for extension, raising head to the sky, about the mediolateral axis.

Table 9: Model Parameter Values

Torsional spring constant ($\frac{N \cdot m}{rad}$)				Torsional damping constant ($\frac{N \cdot m \cdot s}{rad}$)			
K_x	K_{ye}^*	K_{yf}^*	K_z	D_x	D_{ye}^*	D_{yf}^*	D_z
0.022	0.004	0.09E-5	0.002	2.37	16.71	5.38	0.19

*HIII necks are designed with different physical properties for extension (e) and flexion (f) movement of the neck

5.3 Dynamic Predictions

Based on the dynamic equations for the simplified rigid link model, the components of the predicted generalized forces align with their measured counterparts. Figure 12, is the force and torque profiles of a representative test case; the impact scenario for this figure is a mid-level impact to the parietal segment of the head on the unprotected ATD. Predictions across the entire test matrix align to the measured values with an average NRMSE of 0.06 for all unprotected impact tests and 0.13 for helmeted impact tests.

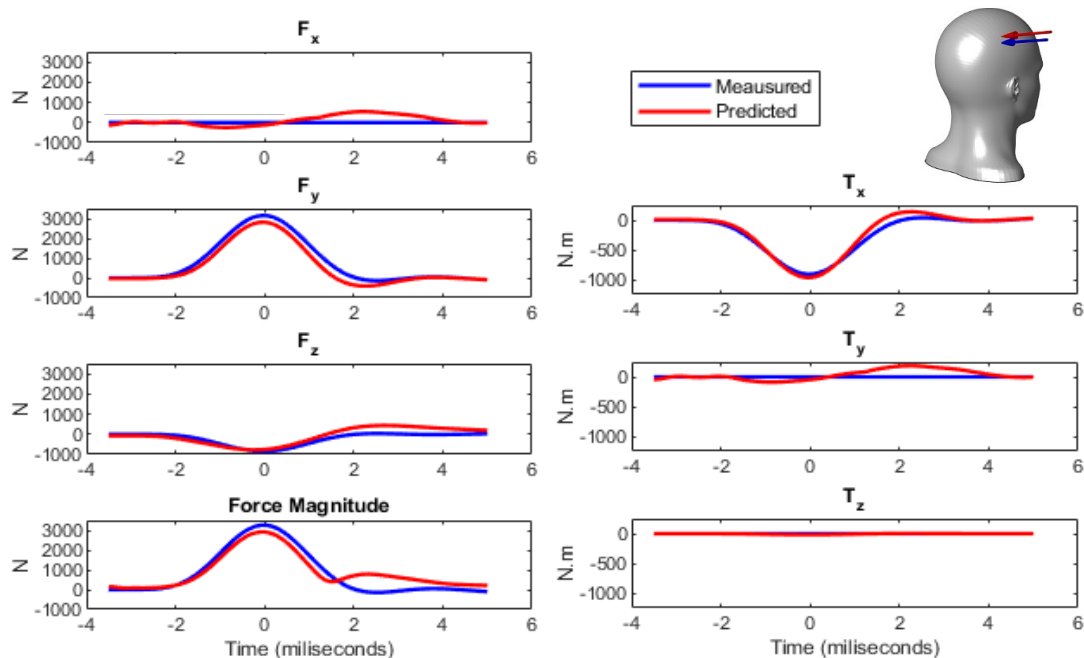


Figure 12: Representative generalized force profiles for rigid body impact

5.3.1 Helmeted Impact Predictions

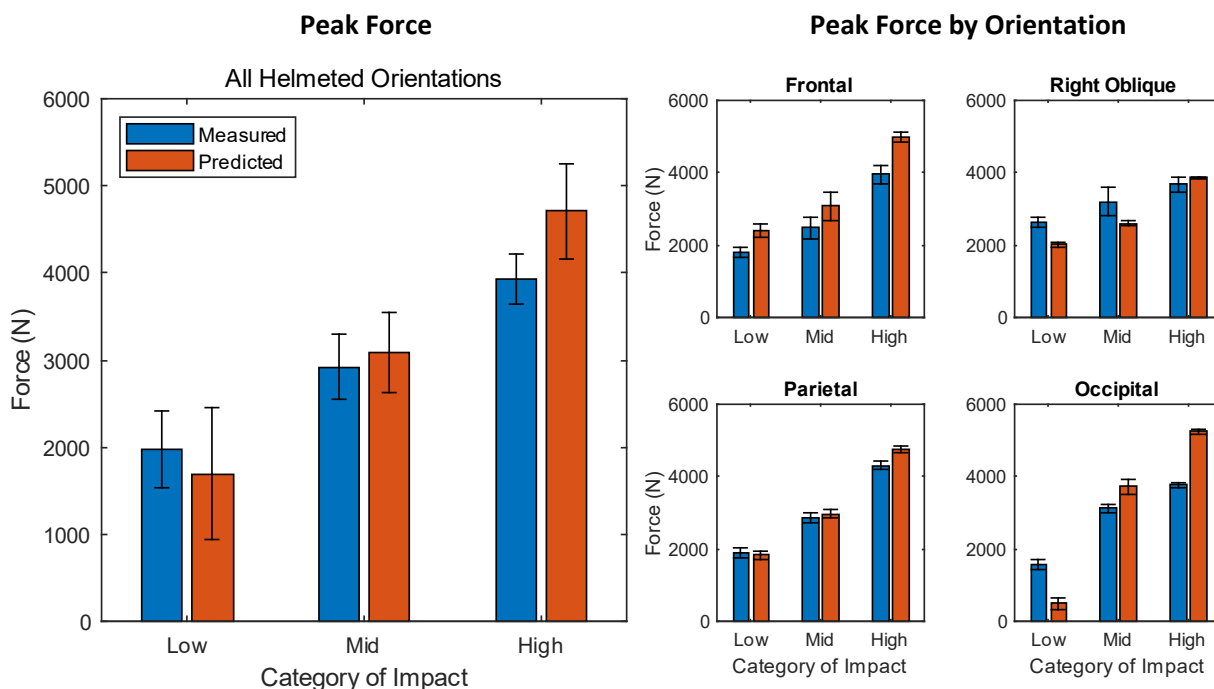


Figure 13: Comparison of measured and predicted peak force magnitudes – helmeted impacts.

The dynamic equations are able to predict peak impact force with a small distribution of errors. As shown in Figure 13, the entire set of helmeted test data shows a tight distribution of predicted to measured impact values; however, when divided by impact orientation there is a larger variation between the ground truth and model results. These variations could be the result of channel errors in data collection, or the fitted model parameters.

With one correcting factor the derived dynamic equations are able to make a good prediction of the applied peak force magnitude. The correcting factor is a coefficient of 0.5 to the derived F_x dynamic equation. Without the correcting factor, forces along the X axis were predicted around 2 times higher than the measured load cell reading for the occipital and frontal orientations. In Figure 13, the low-level occipital impacts are predicted at nearly half of the measured applied force; this leads to the conclusion that the need for the coefficient could be contributed to the pin

connection used as the craniovertebral junction, where the head and neck are attached. For the occipital impact the head rests with the chin resting forward, when applied with low-level impact force there is less depression of the nodding blocks, which would create less contribution from the pin connection. This extra degree of freedom, and point of rotation, is not accounted for in the simplified rigid link model from which the dynamic equations were derived.

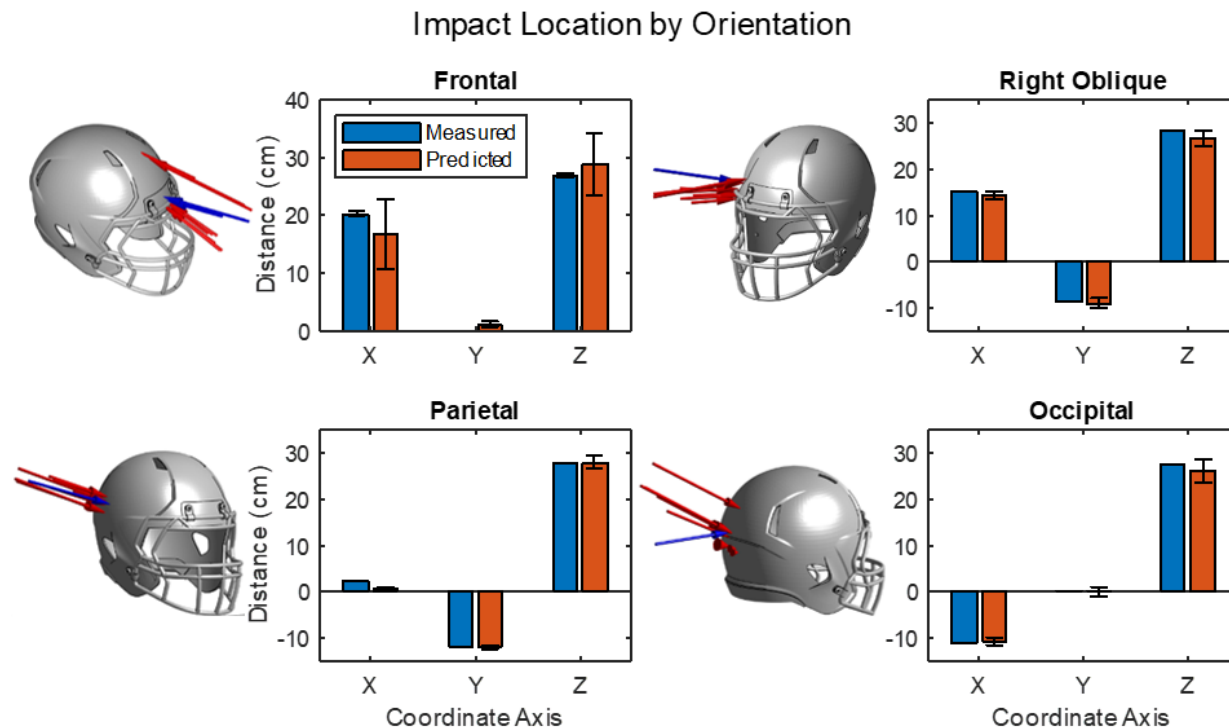


Figure 14: Measured and predicted impact location by orientation of helmeted impacts.

Location of impact was predicted by relating the predicted force from the dynamic equation calculations to the torque calculation through the sum of moment equations (Equations 12-14). Overall, locations of the impact predictions align with the measured values; the largest deviations are seen in the frontal and occipital impact orientations (Figure 14). This could again be a contribution of the pin connection between the head and neck; the largest contribution for torque about the Y axis is force along the X axis, in both the frontal and occipital impact orientations, F_x is the driving component multiplied by distance in the Y direction (R_y).

5.3.2 Unprotected Impact Predictions

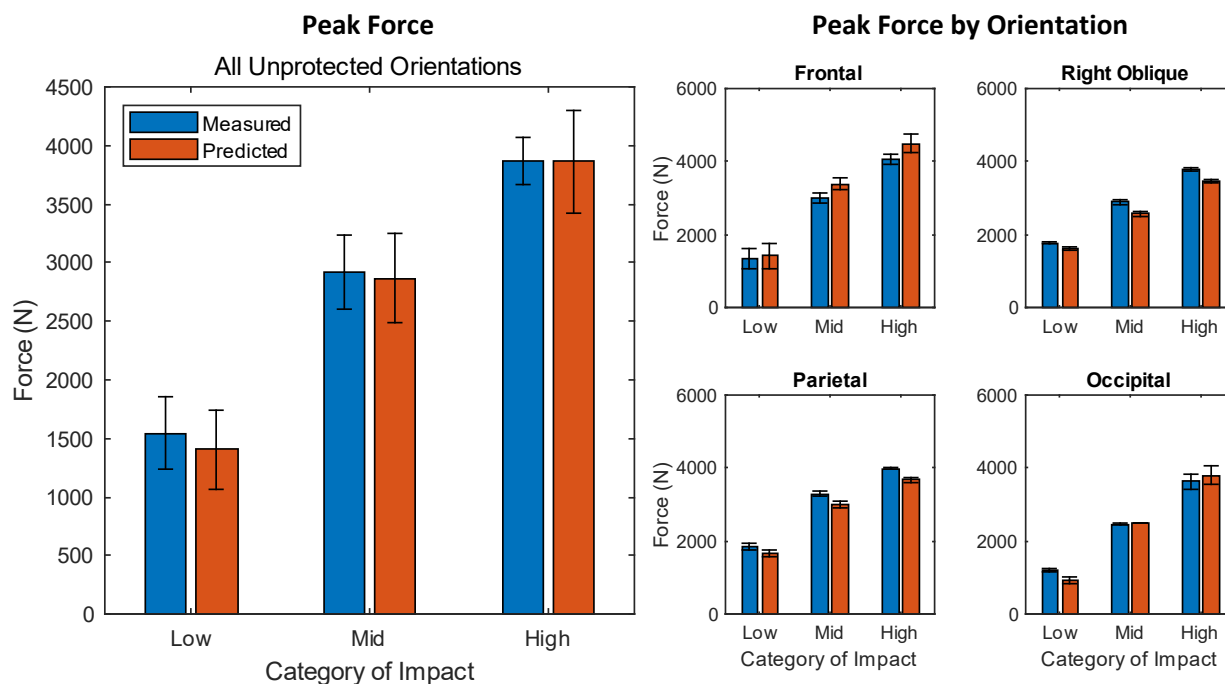


Figure 15: Comparison of measured and predicted peak force magnitudes – unprotected impacts.

The predictions of peak impact force for the unprotected test conditions show similar trends to the helmeted test impacts; however, with the unprotected impacts the distributions of errors is tighter (Figure 15). This could be contributed to the material properties of the NOCSAE head form being constant about the entire head form, whereas the football helmet design dampens applied force differently with each impact orientation.

As with the helmeted impacts, the unprotected impacts required a correcting coefficient to the F_x equation to provide an adequate fit to the experimental data; however, the coefficient used for the unprotected scenarios was higher, 0.7. This higher value for the coefficient strengthens the assumption that the correction is necessary because the head-neck pin connection was neglected when building the simplified rigid link model. Lower impact energy was applied for the

unprotected impact (lower pendulum mass and drop angle), therefore there would be less depression of the rubber nodding blocks.

The locations of impact predicted for the unhelmeted conditions are a good representation of the measured location of impact. Conversely to helmeted impact orientations, frontal and occipital impact location predictions are tightly grouped, whereas right oblique, and parietal impact are more distanced from test to test (Figure 16). This could be due to the corrections made to the mass moment of inertia about the X, anteroposterior, axis. To fit better predictions, I_x for parietal, frontal, and occipital impacts was scaled by 2 from the initial fit value; to better predict for right oblique, I_x was scaled by 5. I_x is a large contributor in the calculation for torque about the X axis.

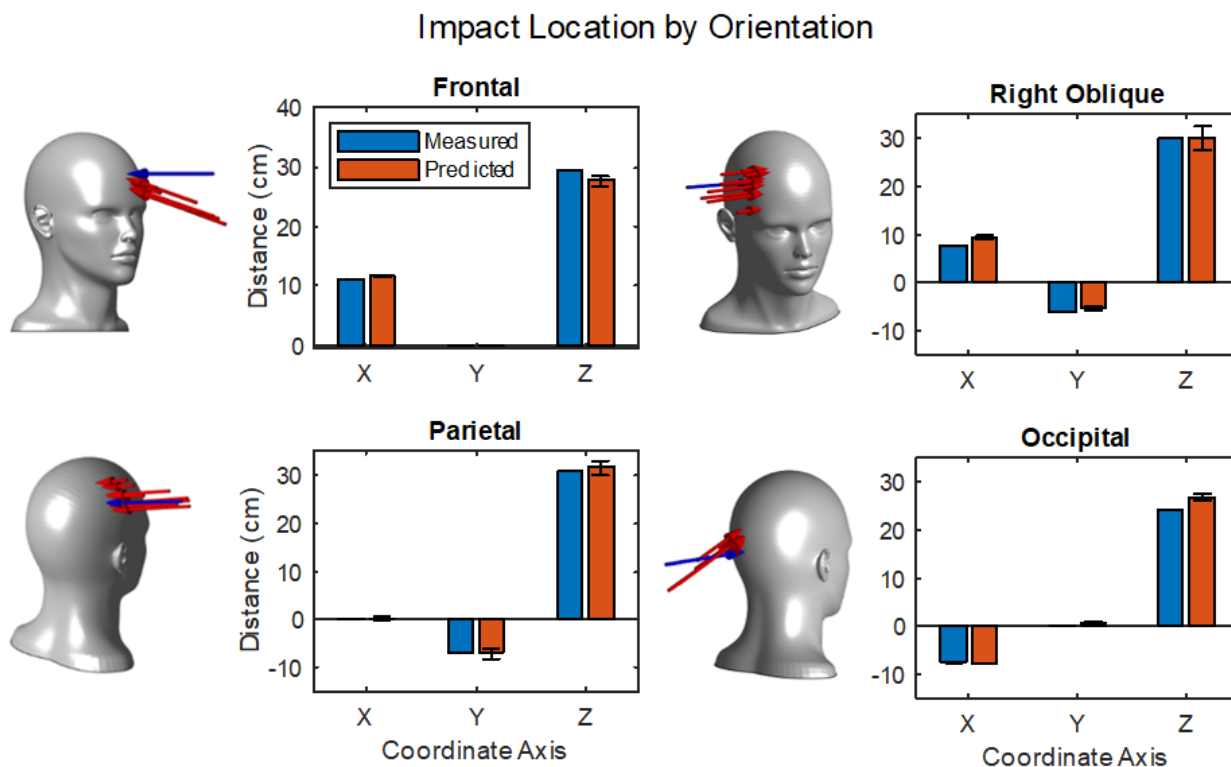


Figure 16: Measured and predicted impact location by orientation of unprotected impacts.

5.3.3 Statistical and Error Analysis

For final data comparison, force from resolved components of load cell readings and torque calculated from Equations 12-14, using resolved force readings and measured impact coordinates, acted as ground truth values. Final force prediction characteristics where the magnitude, direction, and location of impact force. Normalized root mean square error (NRMSE) was used to compare the error of the time series profiles and location of impact. NRMSE was selected due to the vast difference in scale between different predicted values. Kolmogorov-Smirnov (KS) statistical analysis, and cosine similarity were used to compare the predicted force characteristics to the measured applied force. The KS test was chosen because it is a non-parametric test; after exploratory analysis the data did not seem to fit to a normal distribution.

Across all impact scenarios the p-value obtained from the Kolmogorov-Smirnov test comparing the predicted versus actual value is 0.85 for both helmeted and unprotected impact conditions. Given this p-value the test fails to reject the null hypothesis that the distribution of measured and predicted impact force magnitudes come from the same underlying distribution. The standardized empirical cumulative function plots can be found in Appendix IV.

Table 10, shows the NRMSE between the predicted and measured impact characteristics averaged over all impact orientations and tests of each impact scenario; it also includes the average cosine similarity between the impact vectors and the p-values obtained from the KS test. A full table of NRMSE and cosine similarity for all impact orientations and scenarios can be found in Appendix IV. Of the 3 components of the force vector, predicted F_z has the largest variation from its measured counterpart: NRMSE of 0.15 and 0.14 for helmeted and unprotected conditions, respectively. The rotation of the head about the head-neck pin connection may contribute to these higher deviations of the F_z component of force; when force is applied to the frontal and occipital

orientations there is significant movement of the head about the head-neck pin connection. Force was applied with no tilt of the head with respect to impact for frontal and occipital impacts, to reduce contribution from F_z , however; frontal impacts yield high linear acceleration along the +Z axis, and a comparatively large F_z . Similarly occipital impacts yield a high linear acceleration along -Z axis. This spike in F_z can be seen in the deviation in angle of impact. A larger table of NRMSE and cosine similarity results can be found in Appendix IV, Supplementary Data, for each orientation of testing.

Table 10: Comparison of predicted force characteristics to measured, averaged over all impact orientations per Condition.

Impact Condition	Normalized Root Mean Square Error										Cosine Similarity	Peak Force P-Value
	Force				Location			Torque				
	F _x	F _y	F _z	F	R _x	R _y	R _z	τ_x	τ_y	τ_z		
Helmeted	0.06	0.05	0.15	0.17	0.05	0.05	0.15	0.06	0.06	0.14	0.95	0.85
Unprotected	0.04	0.04	0.14	0.15	0.04	0.06	0.19	0.04	0.04	0.06	0.97	0.85

CHAPTER 6: Discussion

6.1 Discussion

Overall, the dynamic equations derived from the Lagrange equations of motion of the simplified rigid link model yield good predictions of the generalized forces acting on the ATD from kinematics collected during impact testing. From these generalized forces, good predictions of impact characteristics, force magnitude, direction, and location are obtained. The discrepancies between the ground truth impact measurements and their predicted characteristics could be contributed to the physical properties of the ATD model, the simplification of the rigid link model, and the design of the protective American football helmet.

The mass moment of inertia, spring constant, and viscous damping constants used in the derived dynamic equations were fitted to the experimental data to minimize the RMSE between the actual and predicted results. Given the number of test sets used to fit the data ($n = 9$), there could be discrepancies between the actual values and the fitted parameters. No calculations were made to calculate off-diagonal terms of the mass moment of inertia matrix, nor were these terms accounted for in the final dynamic equations. While widely used, there are limited resources available outlining inertial properties of the NOCSAE head form or American football helmets. The properties used for this study were fit to the acquired test data and may not be representative of actual values.

The rigid link model used to derive the dynamic equations is simplified; while the ATD device accounts for the craniovertebral junction with a pin connection, the mathematical model assumes a rigid link between the junction of the head and neck. This extra degree of freedom is the suspected cause of increased force predictions along the X axis of the model. At lower impact

energies, the correcting factor is not necessary, which could be attributed to less depression of the rubber nodding blocks and therefore smaller motion about the pin connection.

The protective design of the football helmet is also suspected of adding some discrepancy between the measured characteristics of impact and those predicted by the model. This suspicion stems from the development of the test matrix, the impact energy applied for each category of impact for helmeted scenarios varies slightly to yield measured impact force profiles within the same bounds. It was seen that higher force profiles were seen in the occipital impact cases than frontal cases when applied with the same impact energy (pendulum mass and drop angle). Thus, the design and force damping characteristics of the helmet vary on impact condition and could contribute to the discrepancies in force magnitude seen across the different helmeted impact orientations.

6.2 Limitations

Limitations for this study include the biofidelity of the ATD, simplification of the rigid link model, defined model parameters, and the range of the load cell sensor. The biggest limitation is the biofidelity of the ATD; the HIII neck and NOCSAE head form are only representative and do not capture all the properties or range of motion of the human body. The target table's sliding target mount adds some mass to be representative of a torso, however, the target table only allows for one-degree linear translation, where the human body can move in any direction in response to impact. The rigid link model used to describe the head and neck connection is a simplification of the actual connections between the C7 vertebrae and the craniovertebral junction. Further limitations include the defined model parameters which were fit to experimental data and not defined independently of the rigid link model. Representative impacts did not reach threshold

kinematics of concussion due to the maximum load limit of the load cell sensor; thus, impacts remained within sub-concussive ranges.

6.3 Future Directions

This research could be improved upon by either simplifying the ATD to match with the rigid link model, or to expand the simplified rigid link model to account for the extra degree of freedom introduced by the head-neck pin connection. Further testing needs to be conducted on the NOCSAE head form and the ATD set up together to better determine the physical and inertial properties of the test devices; better representations of these constants would yield better model results.

To expand on the model's prediction capabilities a wider variety of locations of impact should be explored, such as impacts to the rear boss, facemask, and top of the head, as well as varying the direction of force applied to the ATD. The model would also benefit from real-world data obtained from human test subjects. Expanding the data set for analysis could only lead to improvements of the model.

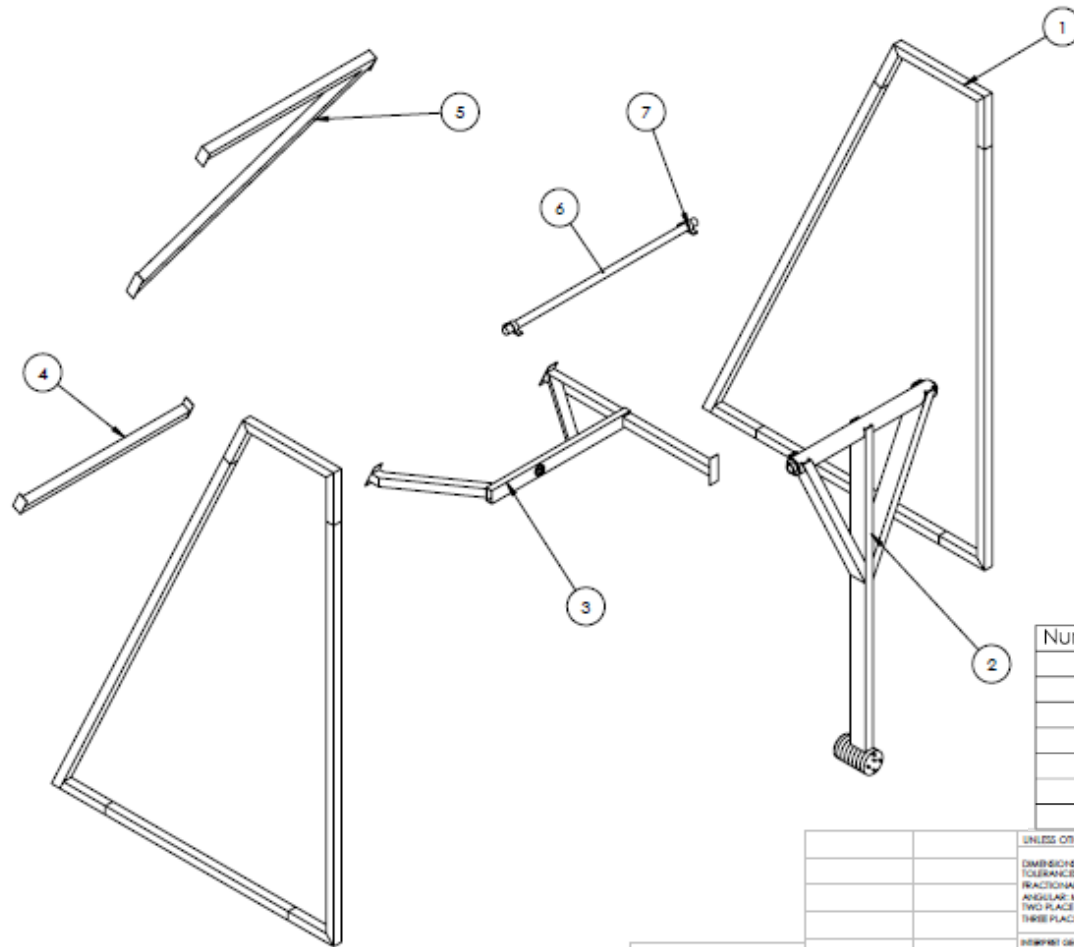
CONCLUSION

It has been shown that rotational and linear kinematic motions of the head are responsible for the deformation of the brain during impact [26]. Cadaver studies and finite element simulations have shown that abrupt motion of the head causes strain and stress to propagate through brain tissue; this tissue deformation is correlated to injury [16], [17], [45]. The greatest influences on generating kinematic motion of the head, leading to brain deformation and risk of injury, are the location, direction, and magnitude of the impacting force [28]. One way to better understand the mechanism of impact, inform return-to-play decisions and develop better protective equipment is to solve the reverse dynamic problem and relate the resultant kinematic motion of the head to the applied generalized forces.

The focus of this research was to replicate impact conditions of contact sports, within a known coordinate reference and to predict location, direction and magnitude of impact force. After conducting representative impacts on an ATD using a custom designed pendulum, developing dynamic equations of motion of a rigid link model, and comparing the predicted force characteristics to measured ground truth, this research shows that it is possible to relate kinematic motion of the head to the applied force characteristics within acceptable error bounds.

Appendix I

Pendulum Assembly



Number	Description	Quantity
1	Side Frame	2
2	Pendulum Arm	1
3	Shock Absorber Support	1
4	Lower Frame Support	1
5	Upper Frame Support	1
6	Steel Rod	1
7	U Clamp	2

PROPRIETARY AND CONFIDENTIAL
 THE INFORMATION CONTAINED IN THIS
 DRAWING IS THE SOLE PROPERTY OF
 ©HONEYWELL INTERNATIONAL INC. ANY
 REPRODUCTION IN PART OR AS A WHOLE
 WITHOUT THE WRITTEN PERMISSION OF
 ©HONEYWELL INTERNATIONAL INC. IS
 PROHIBITED.

UNLESS OTHERWISE SPECIFIED:		NAME	DATE
DIMENSIONS ARE IN INCHES		DRAWN	
TOLERANCES:		CHECKED	
FRACTIONAL		ENG APPR.	
ANGULAR MATCH \pm MIND \pm		MFG APPR.	
TWO PLACE DECIMAL \pm		Q.A.	
THREE PLACE DECIMAL \pm		COMMENTS:	
SHORTEST GEOMETRIC TOLERANCING PER NATIONAL PRACTICE			
NEXT ASST	USED ON		
APPLICATION	DO NOT SCALE DRAWING		

TITLE: Exploded Assembly		
SIZE B	DWG. NO. Full Pendulum Assem	REV
SCALE: 1:48	WEIGHT:	SHEET 2 OF 18

Appendix II

Deriving Euler-Lagrange Dynamics

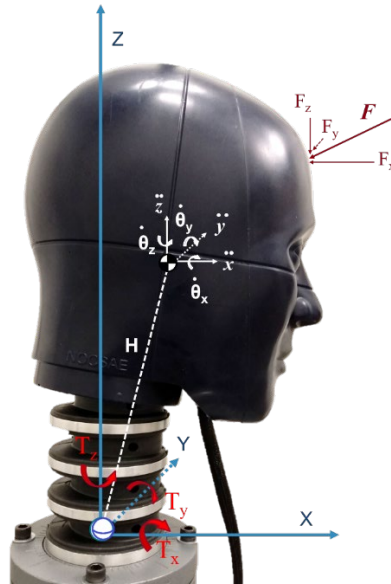


Figure 17: Rigid link manipulator model, coordinate system and generalized forces of ATD.

Alternate Euler-Lagrange:

$$\frac{d}{dt} \left(\frac{\partial T}{\partial \dot{q}_i} \right) - \frac{\partial T}{\partial q_i} + \frac{\partial D}{\partial \dot{q}_i} + \frac{\partial U}{\partial q_i} = Q_i \quad , i = 1, 2, \dots, n \quad (1)$$

Position variables:

$$q = \begin{bmatrix} x \\ y \\ z \\ \theta_x \\ \theta_y \\ \theta_z \end{bmatrix}$$

Velocity variables:

$$\dot{q} = \begin{bmatrix} \dot{x} \\ \dot{y} \\ \dot{z} \\ \dot{\theta}_x \\ \dot{\theta}_y \\ \dot{\theta}_z \end{bmatrix}$$

Generalized forces:

$$Q = \begin{bmatrix} F_x \\ F_y \\ F_z \\ \tau_x \\ \tau_y \\ \tau_z \end{bmatrix}$$

Kinetic energy:

$$T = \frac{1}{2} m_h [\mathbf{V}]^2 + \frac{1}{2} [\mathbf{I}] [\boldsymbol{\omega}]^2$$

Potential energy:

$$U = m_h g z + \frac{1}{2} [\mathbf{K}] [\boldsymbol{\theta}]^2$$

Viscous damping:

$$D = \frac{1}{2} [\mathbf{D}] [\boldsymbol{\omega}]^2$$

Linear velocity:

$$[\mathbf{V}] = \begin{bmatrix} \dot{x} \\ \dot{y} \\ \dot{z} \end{bmatrix}$$

Cartesian - spherical coordinate relation:

$$x = H \cos \theta_z \sin \theta_y, \quad y = H \sin \theta_z \sin \theta_y, \quad z = H \cos \theta_y$$

Linear velocity in spherical coordinates:

$$[\mathbf{V}] = \begin{bmatrix} \dot{x} + H \cos \theta_z \cos \theta_y \dot{\theta}_y - H \sin \theta_z \sin \theta_y \dot{\theta}_z \\ \dot{y} + H \sin \theta_z \cos \theta_y \dot{\theta}_y - H \cos \theta_z \sin \theta_y \dot{\theta}_z \\ \dot{z} - H \sin \theta_y \dot{\theta}_y \end{bmatrix}$$

Angular velocity:

$$[\boldsymbol{\omega}] = \begin{bmatrix} \dot{\theta}_x \\ \dot{\theta}_y \\ \dot{\theta}_z \end{bmatrix}$$

Mass moment of inertia:

$$[\mathbf{I}] = \begin{bmatrix} I_x \\ I_y \\ I_z \end{bmatrix}$$

Torsional Stiffness – Spring Constant:

$$[\mathbf{K}] = \begin{bmatrix} K_x \\ K_y \\ K_z \end{bmatrix}$$

Viscous damping:

$$[\mathbf{D}] = \begin{bmatrix} D_x \\ D_y \\ D_z \end{bmatrix}$$

Mass moment of inertia tensor includes the mass moment of inertia of both the head and neck of the ATD, and helmet, when necessary.

Total kinetic energy of rigid link model:

$$T = \frac{1}{2} m_h \begin{bmatrix} \dot{x} + H \cos \theta_z \cos \theta_y \dot{\theta}_y - H \sin \theta_z \sin \theta_y \dot{\theta}_z \\ \dot{y} + H \sin \theta_z \cos \theta_y \dot{\theta}_y - H \cos \theta_z \sin \theta_y \dot{\theta}_z \\ \dot{z} - H \sin \theta_y \dot{\theta}_y \end{bmatrix}^2 + \frac{1}{2} \begin{bmatrix} I_x \\ I_y \\ I_z \end{bmatrix} \begin{bmatrix} \dot{\theta}_x \\ \dot{\theta}_y \\ \dot{\theta}_z \end{bmatrix}^2$$

Total potential energy of rigid link model:

$$U = m_h g H \cos \theta_y + \frac{1}{2} \begin{bmatrix} K_x \\ K_y \\ K_z \end{bmatrix} \begin{bmatrix} \theta_x \\ \theta_y \\ \theta_z \end{bmatrix}^2$$

Total viscous damping of rigid link model:

$$D = \frac{1}{2} \begin{bmatrix} D_x \\ D_y \\ D_z \end{bmatrix} \begin{bmatrix} \dot{\theta}_x \\ \dot{\theta}_y \\ \dot{\theta}_z \end{bmatrix}^2$$

The derivations of each term, kinetic and potential energy, and viscous damping, was derived according to the alternate Lagrangian (Eq. 1) using MATLAB's live script and derivation functions, then simplified to the final generalized force equations (Eq. 5-10)

Appendix III

FIR Design Filter Derivative

In order to capture a better derivative of the angular velocity signal MATLAB's "designfilt" function which enables the user to design an FIR differentiator. After observing the Welch power spectral density estimate of the angular velocity signals (Figure 17a) the bulk of the signal response lies below 1000 Hz. The differentiator filter was designed with a band pass frequency of 1000 Hz and a stop pass frequency of 1200 Hz; the filter order used was 250. The zero-phase response of the signal is shown in, Figure 17b.

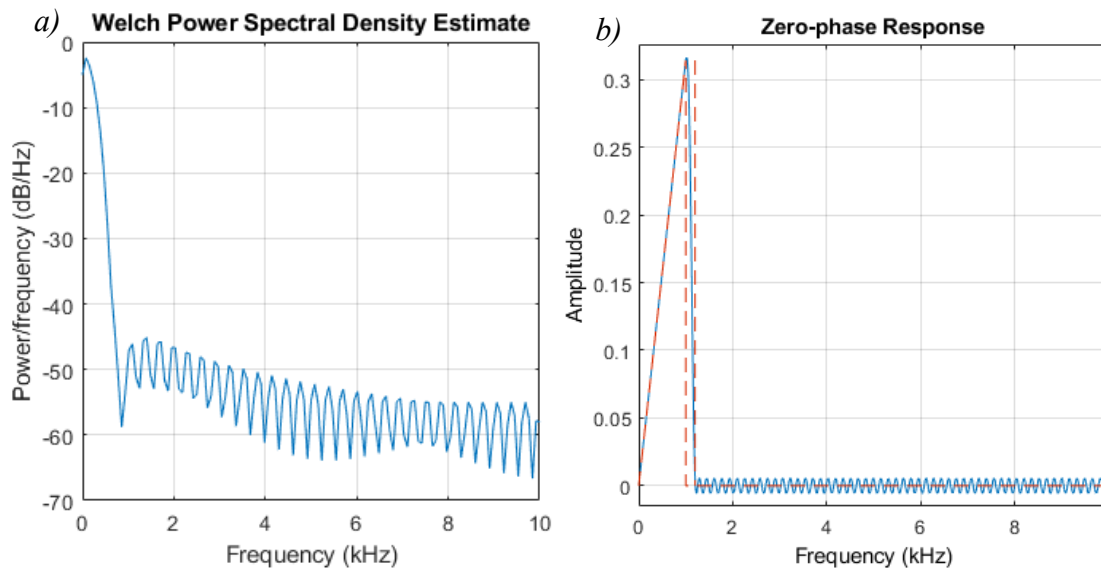


Figure 18: Observations of FIR differentiator filter of angular velocity – a) Welch power spectral density
b) Zero-phase response

Using MATLAB's "filter" function the angular acceleration was derived from angular velocity with the designed filter. A delay occurs when the derivative is taken and an adjustment for the delay was accounted for, aligning the angular velocity and acceleration channels, all other channels were also adjusted to account for the delay.

Defining location of impact

The location of impact must occur on the surface of the ATD; as described in Section 4.4, a representative surface geometry of the NOCSAE head form was designed in SOLIDWORKS, and an open-source geometry file of a Riddell helmet was obtained from GRABCAD (Cambridge, MA) [42]. Figure 19, shows the renderings of the surface geometries used for impact location analysis.

The surface geometries are comprised of an array of x, y, z coordinates, possible locations for head contact. The predicted force vector components (F_x , F_y , F_z) and the surface geometry array coordinates (R_x , R_y , R_z) were used as the inputs to solve for predicted torque (Eq.15). Cosine similarity (Eq. 16) was used to compare the predicted torque to torque calculated from the dynamic equations. The points with the highest cosine similarity were selected for exposure to a logic gate and final selection.



Figure 19: Surface geometries used to define impact location points. SOLIDWORKS renderings. Helmet geometry from [42].

The selection of coordinate points with the highest cosine similarity included points on the head which would yield the kinematic response with a pushing force contact, but also points which yield the same response with a pulling force contact (Figure 19a). This proves to be a problem as the focus of research is to determine the location of impact from a pushing contact force. A logic series was developed to constrain the possible points of impact to pushing contact locations.

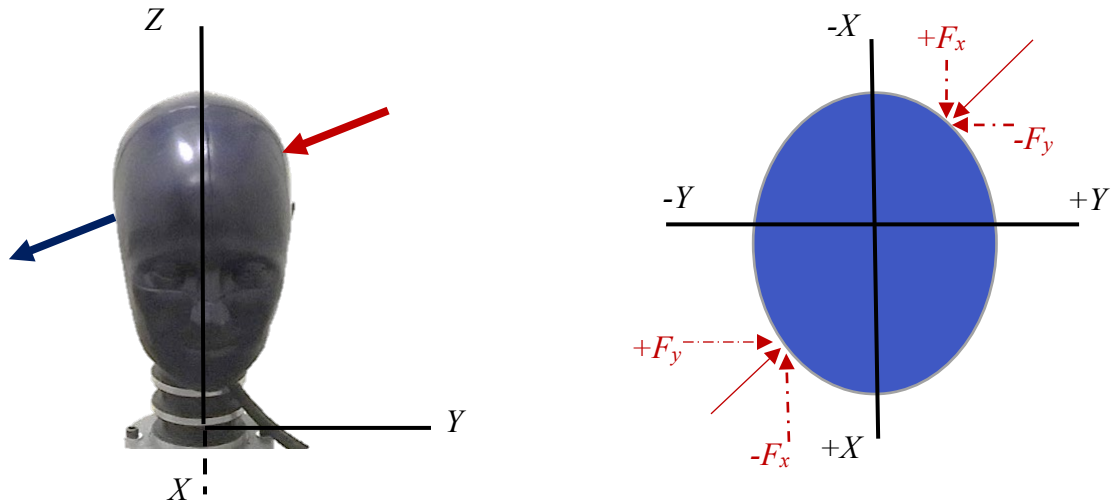


Figure 20: Constraining impact location to a coordinate of pushing contact. a) Example of pushing contact (red) and pulling contact (blue) which would yield a similar kinematic response. b) Coordinate system for logic gate constraints.

Referring to, Figure 19b, the sign (+/-) of the force vector component is opposite of the corresponding position coordinate, e.g., an impact force to the front right oblique region of the head has a negative force component along the X axis, and a positive force component along the Y, the location of impact however, is a coordinate with positive x, and negative y, components. For every location there is a positive z, component. To distinguish impact locations that occur along or near one of the coordinate axes, the logic gate accounts for the magnitude relation of the vector components. The expanded logic statement can be found below.

if $|F_x| > |F_y|$ & $F_x > 0$, then $R_x < 0$; all possible geometry points with $R_x > 0$ are discarded

else if $|F_x| > |F_y|$ & $F_x < 0$, then $R_x > 0$; all possible geometry points with $R_x < 0$ are discarded

else if $|F_y| > |F_x|$ & $F_y > 0$, then $R_y < 0$; all possible geometry points with $R_y > 0$ are discarded

else $|F_y| > |F_x|$ & $F_y < 0$, then $R_y > 0$; all possible geometry points with $R_y < 0$ are discarded

Appendix IV

Exploratory Data Analysis

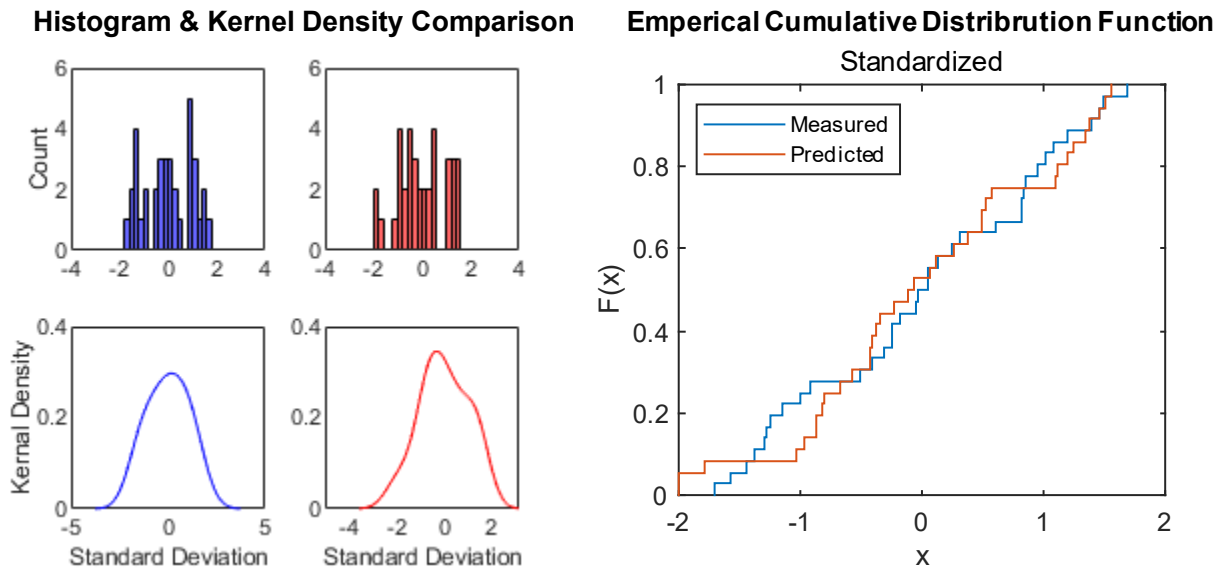


Figure 21: Visual comparison of predicted and actual helmeted force magnitude data

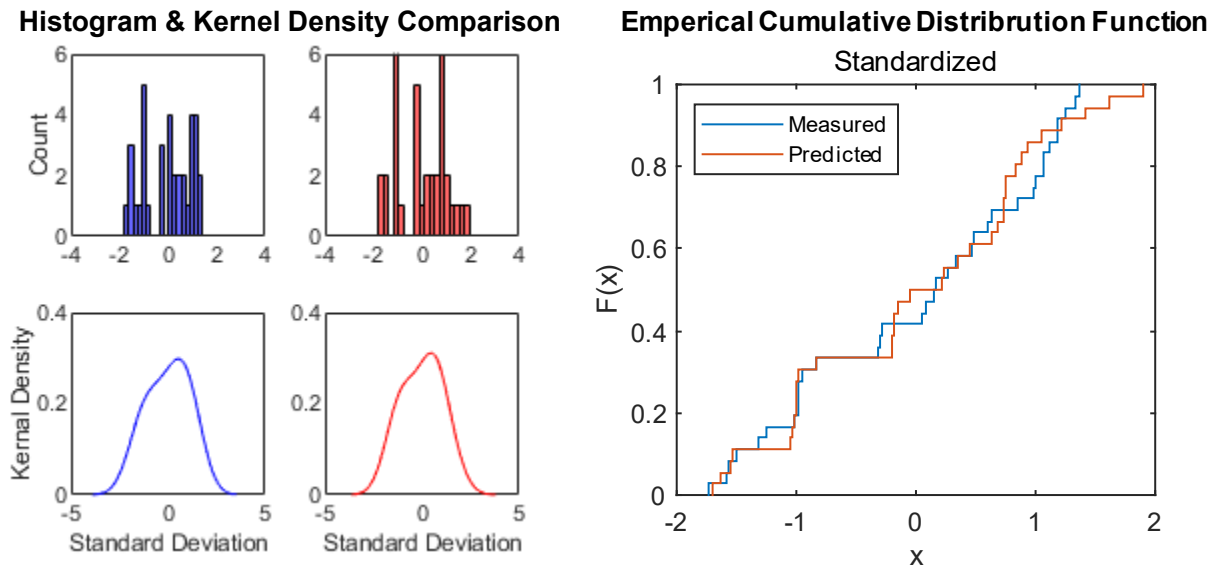


Figure 22: Visual comparison of predicted and actual unprotected force magnitude data

Supplementary Data

Table 11. Comparison of Predicted Impact Characteristics to Measured Test Values by Impact Scenario

		Normalized Root Mean Square Error										Cosine Similarity	
		Force				Location			Torque				
		F _x	F _y	F _z	F	R _x	R _y	R _z	τ _x	τ _y	τ _z		F
Helmetsed Impacts	Frontal	Low	0.05	0.01	0.11	0.12	0.02	0.09	0.08	0.02	0.06	0.07	0.92
		Mid	0.07	0.02	0.19	0.12	0.04	0.03	0.1	0.02	0.08	0.07	0.91
		High	0.09	0.03	0.33	0.21	0.28	0.1	0.57	0.04	0.14	0.11	0.98
	Right Oblique	Low	0.04	0.06	0.08	0.13	0.03	0.07	0.21	0.07	0.03	0.21	0.98
		Mid	0.06	0.09	0.11	0.12	0.03	0.05	0.16	0.1	0.04	0.29	0.98
		High	0.07	0.1	0.17	0.05	0.01	0.06	0.03	0.13	0.05	0.34	0.95
	Parietal	Low	0.02	0.08	0.05	0.01	0.06	0.01	0.07	0.09	0.02	0.11	1
		Mid	0.04	0.09	0.06	0.02	0.04	0.02	0.07	0.1	0.03	0.15	1
		High	0.05	0.13	0.09	0.09	0.04	0.03	0.09	0.13	0.04	0.2	1
	Occipital	Low	0.06	0.01	0.14	0.22	0.01	0.09	0.24	0.01	0.04	0.05	0.97
		Mid	0.06	0.02	0.2	0.12	0.01	0.06	0.05	0.02	0.07	0.06	0.88
		High	0.1	0.01	0.28	0.3	0.04	0.02	0.12	0.01	0.09	0.02	0.87
Unprotected Impacts	Frontal	Low	0.03	0.02	0.1	0.02	0.02	0.03	0.09	0.02	0.03	0.03	0.98
		Mid	0.09	0.02	0.18	0.1	0.04	0.02	0.18	0.02	0.09	0.03	0.97
		High	0.12	0.02	0.24	0.11	0.04	0.01	0.21	0.02	0.12	0.03	0.97
	Right Oblique	Low	0.02	0.03	0.07	0.04	0.1	0.13	0.31	0.04	0.01	0.08	1
		Mid	0.03	0.05	0.11	0.08	0.1	0.07	0.15	0.05	0.02	0.12	1
		High	0.03	0.06	0.15	0.08	0.09	0.05	0.1	0.07	0.02	0.15	1
	Parietal	Low	0.01	0.04	0.06	0.05	0.02	0.1	0.24	0.03	0.02	0.03	0.99
		Mid	0.03	0.07	0.11	0.07	0.01	0.06	0.07	0.07	0.03	0.08	0.99
		High	0.04	0.07	0.12	0.08	0.03	0.09	0.05	0.08	0.04	0.09	0.99
	Occipital	Low	0.03	0.01	0.08	0.07	0.01	0.1	0.27	0.01	0.01	0.03	0.92
		Mid	0.03	0.01	0.18	0.01	0.01	0.06	0.31	0.01	0.04	0.04	0.94
		High	0.06	0.02	0.26	0.04	0.01	0.02	0.27	0.02	0.07	0.04	0.94

REFERENCES

- [1] PC. A. Taylor, J. M. Bell, M. J. Breiding and L. Xu, "Traumatic Brain Injury–Related Emergency Department Visits, Hospitalizations, and Deaths — United States, 2007 and 2013," *CDC MMWR Surveillance Summaries*, vol. 66, no. 9, pp. 1-16, 2017.
- [2] P. Leo and M. McCrea, "Epidemiology," in *Translational Research in Traumatic Brain Injury*, Boca Raton, CRC Press/Taylor and Francis Group, 2016.
- [3] T. Kay et al., "Definition of Mild Traumatic Brain Injury," *Journal of Head Trauma Rehabilitation*, vol. 8, no. 3, pp. 86-87, 1993.
- [4] Harvard T.H. Chan School of Public Health, "Sports and Health in America," <https://cdn1.sph.harvard.edu/wp-content/uploads/sites/21/2015/06/Sports-and-Health-Report.pdf>, 2015.
- [5] D. Waltzman, L. Womack, K. E. Thomas and K. Sarmiento "Trends in Emergency Department Visits for Contact Sports - Related Traumatic Brain Injuries Among Children - United States 2001-2018," Center for Disease Control and Prevention MMWR, 2020.
- [6] Center for Disease Control and Prevention, "CDC Announces Updated Information to help Physicians Recognize and Manage Concussions Early," CDC Newsroom, 2007.
- [7] J. A. Langlois, W. Rutland-Brown and M. M. Wald, "The Epidemiology and Impact of Traumatic Brain Injury," *Journal of Head Trauma Rehabilitation*, vol. 21, no. 5, pp. 375-378, 2006.
- [8] M. A. Bryan, A. Towhani-Rahbar, R. D. Comstock and F. Rivara, "Sports- and Recreation-Related Concussions in US Youth," *Pediatrics*, vol. 138, no. 1, 2016.
- [9] J. E. Bailes, A. L. Petraglia, B. I. Omalu, E. Nauman and T. Talavage, "Role of subconcussion in repetitive mild traumatic brain injury," *Journal of Neurosurgery*, vol. 119, pp. 1233-1245, 2013.

- [10] E. L. Breedlove et al., "Biomechanical correlates of symptomatic and asymptomatic neurophysiological impairment in high school football," *Journal of Biomechanics*, vol. 45, no. 7, pp. 1265-1272, 2012.
- [11] H. Ling et al., "Mixed pathologies including chronic traumatic encephalopathy account for dementia in retired association football (soccer) players," *Acta Neuropathologica*, vol. 133, pp. 337-352, 2017.
- [12] B. Sauser, "A Helmet That Detects Hard Hits," MIT Technology Review, 10 September 2007. [Online]. Available: <https://www.technologyreview.com/2007/09/10/223860/a-helmet-that-detects-hard-hits/>. [Accessed 19 July 2022].
- [13] R. Jadischke, D. C. Viano, N. Dau, A. I. King and J. McCarthy, "On the Accuracy of the Head Impact Telemetry (HIT) System used in Football Helmets," *Journal of Biomechanics*, vol. 46, pp. 2310-2315, 2013.
- [14] L. C. Wu et al., "In Vivo Evaluation of Wearable Head Impact Sensors," *Annals of Biomedical Engineering*, vol. 44, pp. 1234-1245, 2016.
- [15] J. R Funk et al., "Laboratory Reconstruction of Concussive Helmet-to-Helmet Impacts in the National Football League," *Biomedical Engineering Society*, vol. 48, no. 11, pp. 2652-2666, 2020.
- [16] W. N. Hardy, C. D. Foster, M. J. Mason, K. H. Yang, A. I. King and S. Tasham, "Investigation of Head Injury Mechanisms Using Neutral Density Technology and High-Speed Biplanar X-Ray," *Stapp Car Crash Journal*, vol. 45, pp. 337-368, 2001.
- [17] W. N. Hardy et al., "A Study of the Response of the Human Cadaver Head to Impact," *Stapp Car Crash Journal*, vol. 51, pp. 17-80, 2007.
- [18] Concussion in Sport Group, "Sport Concussion Assessment Tool - 5th Edition," 26 April 2017. [Online]. Available: <https://bjism.bmj.com/content/bjsports/early/2017/04/26/bjsports-2017-097506SCAT5.full.pdf>. [Accessed 21 July 2022].

- [19] Royal College of Physicians and Surgeons of Glasgow, "GCS," 2022. [Online]. Available: <https://www.glasgowcomascale.org/>. [Accessed 21 July 2022].
- [20] H-W. Henn, "Crash Tests and the Head Injury Criterion," *Teaching Mathematics and Its Applications*, vol. 17, no. 4, pp. 162-170, 1998.
- [21] D. H Smith and D. F. Meaney, "Axonal Damage in Traumatic Brain Injury," *The Neuroscientist*, vol. 6, no. 6, pp. 483-495, 2000.
- [22] E. G. Takhounts, M. J. Craig, K. Moorhouse, J. McFadden, "Development of Brain Injury Criterion (BRIC)," *Stapp Car Crash Journal*, vol. 57, pp. 243-266, 2013.
- [23] Z. Bi, "Applications - Solid Mechanics Problems," in *Finite Element Analysis Applications: A systematic Approach*, Academic Press, 2019, pp. 281-339.
- [24] E. J. Sanchez, L. F. Gabler, A. B. Good, J. R. Funk, J. R. Crandall and M. B. Panzer, "A Reanalysis of Football Impact Reconstructions for Head Kinematics and Finite Element Modeling," *Clinical Biomechanics*, vol. 64, pp. 82-89, 2019.
- [25] F.A. Bandak, A. X. Zhang, R. E. Tannous, F. Dimasi, P. Masiello and R. Eppinger, "SIMon: A Simulated Injury Monitor; Application to Head Injury Assessment," in *PROCEEDINGS OF 17TH INTERNATIONAL TECHNICAL CONFERENCE ON THE ENHANCED SAFETY OF VEHICLES. CD ROM*, Amsterdam, 2001.
- [26] K. Bian and H. Mao, "Mechanisms and variances of rotation-induced brain injury: a parametric investigation between head kinematics and brain strain," *Biomechanics and Modeling in Mechanobiology*, vol. 19, pp. 2323-2341, 2020.
- [27] F. Hernandez et al., "Six Degree-of-Freedom Measurements of Human Mild Traumatic Brain Injury," *Biomedical Engineering Society*, vol. 43, no. 8, pp. 1908-1934, 2015.
- [28] B. S. Elkin, L. F. Gabler, M. B. Panzer and G. P. Siegmund, "Brain tissue strains vary with head impact location: A possible explanation," *Clinical Biomechanics*, vol. 64, pp. 49-57, 2019.

- [29] P. A. Cripton, D. M. Dressler, C. A. Stuart, C. R. Dennison and D. Richards, "Bicycle helmets are highly effective at preventing head injury during head impact: Head-form accelerations and injury criteria for helmeted and unhelmeted impacts," *Accident Analysis & Prevention*, vol. 70, pp. 1-7, 2014.
- [30] Biokinetics, "biokinetics.com," August 2019. [Online]. Available: https://biokinetics.com/images/stories/Biokinetics_Linear_Impactor_Datasheet_20190801.pdf. [Accessed 27 June 2022].
- [31] E. J. M. Pellman, D. C. Viano, C. Withnall, N. Shewchenko, C. A. Bir and P. D. Halstead, "Concussion in Professional Football: Helmet Testing to Assess Impact Performance—Part 11," *Neurosurgery*, vol. 58, no. 1, pp. 78-96, 2006.
- [32] B. Rowson, S. Rowson and S. M. Duma, "Hockey STAR: A Methodology for Assessing the Biomechanical Performance of Hockey Helmets," *Annals of Biomedical Engineering*, vol. 43, no. 10, pp. 2429-2443, 2015.
- [33] B. R. Cobb, A. MacAlister, T. J. Young, A. R. Kemper, S. Rowson and S. M. Duma, "Quantitative comparison of Hybrid III and National Operating Committee on Standards for Athletic Equipment headform shape characteristics and implications on football helmet fit," *Journal of Sports Engineering and Technology*, vol. 229, no. 1, pp. 39-46, 2015.
- [34] National Football League and National Football League Players Association, "2022 Helmet Laboratory Testing Performance Results," National Football League, 24 March 2022. [Online]. Available: <https://www.nfl.com/playerhealthandsafety/equipment-and-innovation/equipment-testing/helmet-laboratory-testing-performance-results>. [Accessed 19 June 2022].
- [35] R. P. Paul, *Robot Manipulators: Mathematics, Programming, and Control*, Cambridge, Massachusetts: The MIT Press, 1981.
- [36] M. Fanton, C. Kuo, J. Sganga, F. Hernandez and D. B. Camarillo, "Dependency of Head Impact Rotation on Head-Neck Positioning and Soft Tissue Forces," *IEEE Transactions on Biomedical Engineering*, vol. 66, no. 4, pp. 988-999, 2019.

- [37] E. J. Pellman, D. C. Viano, A. M. Tucker and I. R. Casson, "Concussion in Professional Football: Location and Direction of Helmet Impacts - Part 2," *Neurosurgery*, vol. 53, no. 6, pp. 1328-1341, 2003.
- [38] J. J. Crisco et al., "Frequency and Location of Head Impact Exposures in Individual Collegiate Football Players," *Journal of Athletic Training*, vol. 45, no. 6, pp. 549-559, 2010.
- [39] A. E. Jansen, M. McGrath, S. Samorezov, J. Johnston, A. Bartsch and J. Alberts, "Characterizing Head Impact Exposure in Men and Women During Boxing and Mixed Martial Arts," *Orthopaedic Journal of Sports Medicine*, vol. 9, no. 12, 2021.
- [40] J. R. Funk, R. E. Quesada, A. M. Miles and J. R. Crandall, "Inertial Properties of Football Helmets," *Journal of Biomechanical Engineering*, vol. 140, no. 6, 2018.
- [41] I. Kaleps and J. Whitestone, "Hybrid III Geometrical and Inertial Properties," *SAE Transactions*, vol. 97, pp. 107-127, 1988.
- [42] J. Tadic, "GRABCAD Community," 23 10 2013. [Online]. Available: <https://grabcad.com/library/football-helmet-1>. [Accessed 6 July 2022].
- [43] S. Rowson et al., "Rotational Head Kinematics in Football Impacts: An Injury Risk Function for Concussion," *Annals of Biomedical Engineering*, vol. 40, no. 1, pp. 1-13, 2012.
- [44] S. Tiernan et al., "Concussion and the Severity of Head Impact in Mixed Martial Arts," *Proceedings of the Institution of Mechanical Engineers, Part H: Journal of Engineering in Medicine*, vol. 234, no. 12, pp. 1472-1483, 2020.
- [45] R. L. Stalnaker, J. W. Melvin, G. S. Nusholtz, N. M. Alem and J. B. Benson, "Head Impact Response," *SAE International*, vol. 86, pp. 3156-3170, 1977.
- [46] Centers for Disease Control and Prevention, "Surveillance Report of Traumatic Brain Injury-related Hospitalizations and Deaths by Age Group, Sex and Mechanism of Injury - United States, 2016 and 2017," Centers for Disease Control and Prevention, U.S. Department of Health and Human Services, 2021.

- [47] Centers for Disease Control and Prevention, "Traumatic Brain Injury and Concussion," Centers for Disease Control and Prevention, U.S. Department of Health and Human Services, 2021.
- [48] L. J. Carroll, J. D. Cassidy, L. Jolm, J. Kraus and V. G. Coronado, "Methodological Issues and Research Recommendations for Mild Traumatic Brain Injury: The WHO Collaborating Centre Task Force on Mild Traumatic Brain Injury," *Journal of Rehabilitation Medicine*, vol. 43, pp. 113-125, 2004.
- [49] L. E. Miller et al., "Characterizing Head Impact Exposure in Youth Female Soccer with a Custom-Instrumented Mouthpiece," *Research in Sports Medicine*, vol. 28, no. 1, pp. 55-71, 2020.
- [50] L. M. Gessel, S. K. Fields, C. L. Collins, R. W. Dick and R. D. Comstock, "Concussions Among United States High School and Collegiate Athletes" *Journal of Athletic Training*. vol. 42, no. 4, pp. 495-503.
- [51] K. Laksari, M. Kurt, H. Babaei, S. Klieven and D. Camarillo, "Mechanistic Insights into Human Brain Impact Dynamics through Modal Analysis," *Physical Review Letters*, vol. 120, no. 13, pp. 138101-138108, 2018.
- [52] B. Follmer, R. A. Dellagrana and E. P. Zehr, "Head Trauma Exposure in Mixed Martial Arts Varies According to Sex and Weight Class," *Sports Health A Multidisciplinary Approach*, vol. 11, no. 3, pp. 280-285, 2019.